



**HAL**  
open science

## **Poleward shift in the Southern Hemisphere westerly winds synchronous with the deglacial rise in CO<sub>2</sub>**

William Robert Gray, Casimir de Lavergne, Robert Wills, Laurie Menviel, Paul Spence, Mark Holzer, Masa Kageyama, Elisabeth Michel

### ► **To cite this version:**

William Robert Gray, Casimir de Lavergne, Robert Wills, Laurie Menviel, Paul Spence, et al.. Poleward shift in the Southern Hemisphere westerly winds synchronous with the deglacial rise in CO<sub>2</sub>. 2023. <hal-03861919>

**HAL Id: hal-03861919**

**<https://hal.science/hal-03861919v1>**

Preprint submitted on 7 Jun 2023

**HAL** is a multi-disciplinary open access archive for the deposit and dissemination of scientific research documents, whether they are published or not. The documents may come from teaching and research institutions in France or abroad, or from public or private research centers.

L'archive ouverte pluridisciplinaire **HAL**, est destinée au dépôt et à la diffusion de documents scientifiques de niveau recherche, publiés ou non, émanant des établissements d'enseignement et de recherche français ou étrangers, des laboratoires publics ou privés.



Distributed under a Creative Commons CC BY 4.0 - Attribution - International License

This is a non-peer reviewed pre-print submitted to EarthArXiv. This manuscript is currently under review at the journal *Nature*.

Subsequent versions of this manuscript may have slightly different content.

We welcome feedback; please contact William Gray ([william.gray@lsce.ipsl.fr](mailto:william.gray@lsce.ipsl.fr)).

# **Poleward shift in the Southern Hemisphere westerly winds synchronous with the deglacial rise in CO<sub>2</sub>**

William R. Gray<sup>1\*</sup>, Casimir deLavergne<sup>2</sup>, Robert C. J. Wills<sup>3</sup>, Laurie Menviel<sup>4</sup>, Paul Spence<sup>5</sup>, Mark Holzer<sup>6</sup>, Masa Kageyama<sup>1</sup>, Elisabeth Michel<sup>1</sup>

<sup>1</sup>Laboratoire des Sciences du Climat et de l'Environnement (LSCE/IPSL), Université Paris-Saclay, Gif-sur-Yvette, France

<sup>2</sup>LOCEAN Laboratory, Sorbonne Université-CNRS-IRD-MNHN, Paris, France

<sup>3</sup>Department of Atmospheric Sciences, University of Washington, Seattle, WA 98195, USA

<sup>4</sup>Climate Change Research Centre, University of New South Wales, NSW 2052 Sydney, Australia

<sup>5</sup>School of Geosciences, University of Sydney, Sydney, Australia

<sup>6</sup>School of Mathematics and Statistics, University of New South Wales, NSW 2052 Sydney, Australia

\*To whom correspondence should be addressed: william.gray@lsce.ipsl.fr

**The Southern Hemisphere westerly winds strongly influence deep ocean circulation and carbon storage<sup>1</sup>. While the westerlies are hypothesised to play a key role in regulating atmospheric CO<sub>2</sub> over glacial-interglacial cycles<sup>2-4</sup>, past changes in their position and strength remain poorly constrained<sup>5-7</sup>. Here, we use a compilation of planktic foraminiferal  $\delta^{18}\text{O}$  from across the Southern Ocean and constraints from an ensemble of climate models to reconstruct changes in the westerlies over the last deglaciation. We find a 4.7° (2.9-6.9°, 95% confidence interval) equatorward shift and about a 25% weakening of the westerlies during the Last Glacial Maximum (about 20,000 years ago) relative to the mid-Holocene (about 6,000 years ago). Our reconstruction shows that the poleward shift in the westerlies over deglaciation closely mirrors the rise in atmospheric CO<sub>2</sub>. Experiments with a 0.25° resolution ocean-sea-ice-carbon model demonstrate that shifting the westerlies equatorward substantially reduces the overturning rate of the abyssal ocean, leading to a suppression of CO<sub>2</sub> outgassing from the Southern Ocean. Our results establish a central role for the westerly winds in driving the deglacial CO<sub>2</sub> rise, and suggest natural CO<sub>2</sub> outgassing from the Southern Ocean is likely to increase as the westerlies shift poleward due to anthropogenic warming<sup>8-10</sup>.**

The Southern Hemisphere westerly winds play a key role in returning deep ocean waters to the surface and thus largely govern the rate at which the deep oceanic reservoirs of heat and carbon communicate with the surface ocean and atmosphere<sup>1,11</sup>. South of ~47°S the modern westerly winds drive divergent northward Ekman transports in the near-surface ocean that contribute to lift deepwaters and tilt density surfaces<sup>11</sup>. Although mesoscale eddies work to flatten out the steep isopycnals, the counteraction of the wind-driven circulation by the

40 eddies is incomplete, resulting in a residual circulation which brings macro-nutrient and carbon  
41 rich deepwaters to the surface<sup>1,12</sup>. Due to iron<sup>13</sup> and light limitation<sup>14</sup> the upwelled nutrients are  
42 not completely utilised before buoyancy loss close to the Antarctic continent causes some of  
43 the upwelled waters to sink as Antarctic Bottom Water, filling the deep ocean with 'preformed'  
44 nutrients<sup>15</sup>. This 'leak' in the biological pump, largely caused by the over-supply of nutrients to  
45 the surface ocean by the wind-driven upwelling, leads to the hypothesis that changes in the  
46 Southern Hemisphere westerly winds could regulate atmospheric CO<sub>2</sub> over glacial-interglacial  
47 cycles<sup>2-4</sup>. Modelling studies<sup>15-17</sup> indicate a tight coupling between the oceans' preformed  
48 nutrient inventory and atmospheric CO<sub>2</sub>, while proxy data<sup>4,18</sup> indicate large changes in nutrient  
49 supply to the surface of the Southern Ocean over glacial-interglacial cycles.

50

51 Past changes in the position and strength of the Southern Hemisphere westerly winds  
52 are poorly constrained, making it difficult to assess their role in driving past carbon cycle  
53 changes. A recent compilation of diverse proxy data<sup>5</sup> suggested signals of an equatorward  
54 shift in the westerlies during the Last Glacial Maximum (LGM, 19-23 ka) relative to the  
55 Holocene. However, relating changes in the measured proxies (i.e. terrestrial moisture, marine  
56 productivity) back to the position of the westerlies is challenging, both quantitatively and  
57 qualitatively, such that even the direction of change during the LGM (i.e. poleward versus  
58 equatorward) is debated<sup>6,7</sup>. Furthermore, while climate models show a relatively clear and  
59 consistent signal of an equatorward shift in the Northern Hemisphere near-surface westerlies  
60 under glacial forcings<sup>19-21</sup> in good agreement with proxy data<sup>19</sup>, they show little consistency in  
61 the magnitude or sign of change in the Southern Hemisphere<sup>6,20,22</sup>. Ice core data suggest  
62 abrupt shifts in the westerlies during the millennial scale atmospheric CO<sub>2</sub> variability of the last  
63 glacial period<sup>23</sup>, but there is currently very little constraint on how or when the westerlies shifted  
64 over the last deglaciation (20 - 10 ka), as atmospheric CO<sub>2</sub> rose by ~90 ppmv<sup>24</sup>.

65

66 To reconstruct changes in the position of the Southern Hemisphere westerly winds  
67 over the last deglaciation we exploit the coupling between the latitude of the maximum zonal  
68 wind stress (hereafter referred to as *wind latitude*) and the latitude of the maximum meridional  
69 sea surface temperature (SST) gradient (hereafter referred to as *SST front latitude*) in the  
70 Southern Ocean (Fig. 1). This two-way coupling arises through the winds' dependence on the  
71 atmospheric temperature gradient and through the winds' control on ocean circulation, which  
72 together shape the meridional SST profile<sup>25-27</sup>. The position of the peak in westerly wind-speed  
73 coincides with the position of the SST front around much of the modern Southern Ocean,  
74 except where bathymetric steering of ocean currents causes local decoupling<sup>25,28</sup> (Fig 1). An  
75 ensemble of models from the Paleoclimate Modelling Intercomparison Project (PMIP3 and  
76 PMIP4) and Coupled Model Intercomparison Project (CMIP5 and CMIP6) show a tight

77 relationship between the wind latitude and the SST front latitude across pre-industrial, LGM,  
78 and 4xCO<sub>2</sub> simulations (Methods; Fig. 1c). This relationship, stemming from large-scale  
79 atmosphere-ocean coupling, indicates we can use changes in the SST front latitude to  
80 reconstruct past shifts in the wind latitude.

81

82 To track changes in the latitude of the Southern Ocean SST front over the deglaciation  
83 we use a basin-wide compilation of  $\delta^{18}\text{O}$  in planktic foraminiferal calcite ( $\delta^{18}\text{O}_{\text{calcite}}$ ). Although  
84  $\delta^{18}\text{O}_{\text{calcite}}$  is a function of both temperature and the  $\delta^{18}\text{O}$  of seawater ( $\delta^{18}\text{O}_{\text{water}}$ ), the effect of  
85 temperature is around six times greater than the effect of  $\delta^{18}\text{O}_{\text{water}}$  at the basin scale (Extended  
86 Data Fig. 1). As no physical mechanism exists to drive such large changes in  $\delta^{18}\text{O}_{\text{water}}$  at the  
87 basin scale, the meridional pattern of  $\delta^{18}\text{O}_{\text{calcite}}$  will always be dominated by temperature  
88 (Methods). Meridional profiles of  $\delta^{18}\text{O}_{\text{calcite}}$  thus allow us to identify the latitude of the SST front  
89 and ultimately that of the westerly winds.

90

91 We compiled existing records of planktic foraminiferal  $\delta^{18}\text{O}$  from near-surface dwelling  
92 species from core sites across the Southern Ocean and generated new data from the  
93 Kerguelen plateau and southeast Pacific, resulting in a dataset of 64 planktic foraminiferal  
94  $\delta^{18}\text{O}$  records spanning the last deglaciation (Fig. 1a; Extended Data Figs. 2 and 3; Methods).  
95 Meridional shifts in the SST front ( $\Delta\text{Lat}_{\text{SST}}$ ) are calculated by finding the latitudinal shift that  
96 minimises the difference between the Holocene  $\delta^{18}\text{O}$  profile and the profile at each time step  
97 within a 10° latitudinal window that includes the steepest part of the meridional  $\delta^{18}\text{O}$  profile<sup>19</sup>  
98 (Methods; Fig. 1b and Extended Data Figs. 2 and 3). We account for whole ocean changes in  
99  $\delta^{18}\text{O}_{\text{water}}$  and the global-mean SST change ( $\delta^{18}\text{O}_{\text{ivc-gtc}}$ ; Fig. 1a; Extended Data Figs. 2 and 3),  
100 quantifying uncertainties via bootstrapping and Monte-Carlo simulation (Methods). We  
101 compute  $\Delta\text{Lat}_{\text{SST}}$  across the entire Southern Ocean, as well as separately in the Indian-Pacific  
102 and Atlantic sectors (Fig. 2; Extended Data Fig. 4).

103

104 The data reveal an equatorward shift in the SST front during the LGM (20ka) relative  
105 to 10 ka, indicative of an equatorward shift in the westerly winds (Fig. 1b; Extended Data Figs.  
106 2 and 3). Mapping the LGM  $\delta^{18}\text{O}_{\text{ivc-gtc}}$  anomalies shows a large mid-latitude cooling during the  
107 LGM across the Indian and Pacific sectors (Fig. 1a; equivalent to a cooling of 4-5°C beyond  
108 the global-mean SST change). Our Indian-Pacific  $\Delta\text{Lat}_{\text{SST}}$  reconstruction shows a 4.8° (3.6-  
109 6.1° 95% confidence interval [CI]) equatorward shift in the SST front during the LGM relative  
110 to 10 ka (Fig. 2c; Extended Data Fig. 4). We perform a 'leave-one-out' analysis of the Indian-  
111 Pacific dataset which shows that no single record is contributing more than 5% of the total

112 reconstruction and indicates that Indian-Pacific  $\Delta\text{Lat}_{\text{SST}}$  reconstruction primarily reflects a mid-  
113 latitude signal (Methods; Extended Data Fig. 4).

114

115 By contrast, we find a slight warming anomaly (relative to the global-mean LGM SST  
116 change) at all latitudes in the western Atlantic (Fig. 1), possibly a signal of a weakened Atlantic  
117 Meridional Overturning Circulation (AMOC)<sup>29,30</sup>, and no significant change in the SST front  
118 latitude within the Atlantic sector over deglaciation (Extended Data Fig. 4). This result is  
119 consistent with strong bathymetric steering of currents in the Atlantic sector<sup>28</sup>, and the lack of  
120 a modelled relationship between the SST front latitude and wind latitude in this sector,  
121 particularly in the eastern Atlantic where the vast majority of the mid-latitude cores are located  
122 (Fig. 1; Extended Data Fig. 5bc). Although we attribute the lack of change in the SST front  
123 latitude within the Atlantic to the modelled decoupling of the westerlies and SST front there  
124 (Extended Data Fig. 5bc), we cannot rule out that the westerlies did not shift substantially over  
125 deglaciation within the Atlantic.

126

127 We apply the multi-model relationship between the wind latitude and the SST front  
128 latitude in the Indian-Pacific sector (Fig. 2; Extended Data Fig. 5a) to our Indian-Pacific  $\Delta\text{Lat}_{\text{SST}}$   
129 reconstruction and quantify shifts in the zonal-mean wind latitude over the deglaciation  
130 ( $\Delta\text{Lat}_{\text{wind}}$ ). A regional subset test demonstrates that our method is able to track shifts in the  
131 zonal-mean wind latitude using changes in the latitude of regional SST fronts (Fig. 2;  
132 Methods); although different regions yield differing magnitudes of deglacial change in the SST  
133 front latitude (Fig. 2b), they yield almost identical time series of the zonal-mean wind latitude  
134 (Fig. 2d), given the region-specific multi-model relationship between the two variables (Fig.  
135 2c). Measured shifts in the SST front latitude thus provide a robust constraint on the wind  
136 latitude. We find a  $6.2^\circ$  ( $4.4\text{-}8.4^\circ$  95% CI) equatorward shift in the wind latitude during the LGM  
137 (20 ka) relative to 10 ka (Figs. 2d and 3a). The evolution of the wind latitude over deglaciation  
138 closely mirrors, and is highly correlated with, the evolution of atmospheric  $\text{CO}_2$  (ref<sup>24</sup>) (Fig. 3).  
139 A lagged correlation suggests changes in the wind latitude may have led the rise in  
140 atmospheric  $\text{CO}_2$  and global temperature<sup>31</sup> by a few hundred years during certain intervals  
141 over the deglaciation, although difficulties in fully quantifying age uncertainties make this result  
142 tentative (Methods; Fig. 3c).

143

144 Extending our analysis to span a longer time interval (22 to 6.5 ka) indicates an early  
145 Holocene extremum in the poleward position of the westerlies, followed by a  
146  $\sim 1.5^\circ$  equatorward shift in the winds over 10-6.5 ka (Extended Data Fig. 6). Despite the larger  
147 uncertainties in the early Holocene reconstruction, it agrees well with the analysis of the full  
148 dataset (i.e., 10-20 ka) in the overlapping sections (Extended Data Fig. 6). Our results thus

149 indicate a 4.7° (2.9-6.9° 95% CI) equatorward shift of the westerlies during the LGM (20 ka)  
150 relative to the mid Holocene (6.5 ka). Assuming no substantial shift in the westerlies from the  
151 mid- to late- Holocene (Methods), the magnitude of the reconstructed wind shift is substantially  
152 greater than that predicted by any of the models within the PMIP3/4 ensemble between  
153 preindustrial and LGM states (Extended Data Fig. 7). The models show a relationship between  
154 the wind latitude and the maximum magnitude of the zonal-mean zonal wind stress (*wind*  
155 *strength*; Extended Data Fig. 5e), such that the reconstructed shift in wind latitude also implies  
156 a reduction in wind strength of ~25% during the LGM relative to the mid Holocene (Methods;  
157 Extended Data Fig. 8).

158

159 The similarity of the changes in wind latitude and atmospheric CO<sub>2</sub> over the  
160 deglaciation (Fig. 3) reinforces the hypothesis of their coupling through Southern Ocean  
161 circulation and carbon cycling. While modelling studies typically show a consistent increase in  
162 oceanic carbon storage following a weakening of the westerlies, the impact of shifts in the  
163 latitude of the westerlies is more uncertain<sup>17,32</sup>. To better understand how changes in the  
164 latitude of the westerlies may affect the oceanic overturning circulation and carbon cycle, we  
165 performed two experiments with a global ocean-sea-ice-carbon model with 0.25° horizontal  
166 resolution<sup>33,34</sup>: A Control experiment is forced by climatological atmospheric forcing  
167 representative of the recent instrumental period. A Perturbed experiment uses the same  
168 forcing except for a uniform 4° equatorward shift of the Southern Hemisphere westerlies, with  
169 no change in their magnitude (Methods). Both experiments are run for 125 years, starting from  
170 the near-equilibrium control state. As the applied wind stress forcing does not include the  
171 implied 25% reduction in wind strength (and is smaller than our reconstructed LGM shift) this  
172 simulation is not designed to represent our 'best estimate' of LGM Southern Hemisphere wind  
173 stress, but rather represents a conservative estimate which enables us to assess the broad  
174 impacts of an equatorward shift in the westerlies alone. The 125-year transient response of  
175 the system forced by an equatorward shift in the westerlies does not allow quantification of  
176 the equilibrium response of the deep ocean nutrient and carbon cycles<sup>17</sup>. It nevertheless  
177 reveals clear trends in circulation and biogeochemistry which provide an indication of how the  
178 rapidly responding Ekman-driven transport reorganizes the residual circulation, allowing us to  
179 assess how an equatorward shift in the westerlies may qualitatively impact the carbon cycle  
180 on longer timescales.

181

182 We find a complete suppression of CO<sub>2</sub> outgassing south of 60°S in the Perturbed  
183 experiment (Fig. 4), with only a partial compensation further north. As such, there is an  
184 anomalous uptake of 27 GtC by the Southern Ocean south of 35°S over the course of the  
185 Perturbed experiment, equivalent to a CO<sub>2</sub> decrease of 13 ppm (Fig. 4). Deepwater upwelling

186 and surface nutrient and carbon concentrations are substantially reduced south of 60°S (Fig.  
187 4), indicating that reduced exposure of nutrient and carbon rich deepwaters in the polar  
188 Southern Ocean underpins the simulated carbon cycle response to equatorward-shifted  
189 westerlies (Methods). As the winds shift equatorward relative to their modern position,  
190 northward Ekman transports become more divergent north of about 60°S, but less divergent  
191 south of 60°S (Fig. 4). In our simulation, the effect is a substantial decrease in upwelling within  
192 the polar Southern Ocean south of 60°S (Fig. 4) and a pronounced slowdown in the residual  
193 circulation of the abyssal ocean globally (Fig. 5), with the largest reduction within the Pacific  
194 (Extended Data Fig. 9). The decrease in abyssal overturning results in increased storage of  
195 carbon and regenerated nutrients throughout the deep ocean below ~1.5 km, concurrent with  
196 a decrease in dissolved oxygen (Fig. 5c; Extended Data Fig. 10). Conversely, we see an  
197 increase in upwelling north of 60°S and increased overturning at intermediate depths, such  
198 that carbon concentrations decrease in the upper ~1.5 km (Fig. 5c; Extended Data Fig. 10).  
199 Hence, although shifting the winds equatorward increases the overall Ekman divergence  
200 across the Southern Ocean (Fig. 4b), it focuses the wind's energy away from isopycnals  
201 outcropping carbon-rich abyssal waters, toward isopycnals outcropping intermediate waters  
202 containing relatively less carbon (Fig. 5b); these changes are synergistic such that the  
203 concentration of carbon and nutrients within the intermediate depths decreases as the  
204 overturning at these depths spins up. The net effect in the model is an increase in oceanic  
205 carbon storage (Fig 5c). In contrast, some previous studies using coarser-resolution models  
206 simulated a decrease in oceanic carbon content in response to an equatorward shift in the  
207 westerlies<sup>17,32</sup>. We attribute this difference to the response of the residual circulation in the  
208 Southern Ocean, the representation of which should improve at higher resolution<sup>35,36</sup>.

209  
210 Crucially, the reduction in the upwelling of nutrients to the surface of the polar Southern  
211 Ocean lowers the preformed nutrient concentration of Antarctic Bottom Water (Fig. 4;  
212 Extended Data Fig. 10). Preformed nutrient concentrations also decrease in the upper cell  
213 (Methods), such that preformed nutrient concentrations begin to decrease throughout the  
214 deep ocean (Extended Data Fig. 10). The simulated circulation changes with equatorward-  
215 shifted winds thus imply a substantial long-term increase in the efficiency of the biological  
216 pump and decrease in atmospheric CO<sub>2</sub> (Methods; refs<sup>15,16</sup>). In addition to the overall increase  
217 in regenerated nutrients and carbon, the model indicates a redistribution of the regenerated  
218 nutrient and carbon pools toward the abyss (Fig. 5c; Extended Data Fig. 10), such that the  
219 vertical carbon gradient increases. This implies a further reduction atmospheric CO<sub>2</sub> via  
220 carbonate compensation<sup>16,37</sup> (Methods).

221

222 Despite the 4° equatorward shift in the Southern Hemisphere westerlies being the only  
223 perturbation applied, and the short duration of the Perturbed experiment, the sign of the  
224 simulated circulation and carbon cycle changes concurs with proxy observations from the  
225 LGM of a more sluggish abyssal circulation<sup>38</sup>, an increase in regenerated nutrients and carbon  
226 within the deep ocean<sup>39–41</sup> and a redistribution of regenerated nutrients and carbon toward the  
227 abyss<sup>39,40,42</sup>, as well as a shoaling of the AMOC<sup>29</sup> (Fig. 5; Extended Data Fig. 9). The simulated  
228 decrease in nutrient upwelling and export production within the polar Southern Ocean, and  
229 the increase further north (Fig. 4; Extended Data Fig. 10), are also in good agreement with  
230 LGM proxy data<sup>3,5,43</sup>.

231

232 The sign of the simulated trends is unlikely to be contingent on the absence of a  
233 simulated change in atmospheric temperature or on model approximations such as  
234 parameterized eddy effects (Methods). Indeed, the trends directly ensue from changes in  
235 Ekman transports—themselves a function only of wind stress and geometry—and their  
236 position relative to the underlying bathymetry. The northward shift of the Ekman divergence  
237 (Fig. 4b,c) explains the northward shift in upwelling and CO<sub>2</sub> outgassing (Fig. 4d,e; Methods).  
238 This shift does not merely draw the overturning northward but shoals the upper cell and  
239 weakens the abyssal cell (Fig. 5b; Extended Data Fig. 9). This response stems from the  
240 influence of bathymetry on the vertical extent of wind-driven upwelling<sup>11,44</sup>. Specifically, the  
241 presence of a zonally continuous channel at Drake Passage latitudes (56–60°S) above 2 km  
242 depth favors deeper waters as the mass replacement for the surface divergence to its  
243 south<sup>11,45</sup>. Displacement of the Ekman divergence from south of 60°S to lower latitudes thus  
244 suppresses the privileged upwelling pathway of abyssal waters (> 2 km depth) and instead  
245 favors overturning in the upper ocean. Although the representation of surface buoyancy  
246 forcing and mesoscale eddies can affect the response of the overturning to changing  
247 winds<sup>12,44</sup>, the simulated slowdown of the abyssal overturning is a robust consequence of its  
248 bathymetry-driven sensitivity to Ekman flow in the polar Southern Ocean.

249

250 Our results thus suggest that as the winds shifted poleward through the deglaciation,  
251 their ability to lift abyssal waters to the surface increased in approximate proportion to the  
252 northward Ekman transport at 60°S. Using the relationship between wind latitude and the  
253 zonal-mean wind stress at 60°S within the PMIP/CMIP ensemble (Extended Data Fig. 5d;  
254 Extended Data Fig. 8) we estimate that over deglaciation this transport increased from an  
255 LGM minimum of around  $4 \times 10^6 \text{ m}^3 \text{ s}^{-1}$  to a maximum of  $18 \times 10^6 \text{ m}^3 \text{ s}^{-1}$  at 11 ka, before  
256 decreasing back to  $14 \times 10^6 \text{ m}^3 \text{ s}^{-1}$  by the mid-Holocene (Fig. 6a; Methods). This invigoration  
257 of the abyssal overturning over deglaciation would have driven carbon out of the abyssal  
258 ocean and back to the intermediate depths, surface, and atmosphere. This concurs with

259 records of deep Pacific oxygen<sup>41</sup> and deep Southern Ocean pH<sup>39</sup> which suggest of a loss of  
260 regenerated nutrients and carbon from the abyssal ocean over deglaciation (Fig. 6c).  
261 Furthermore, a decrease in the global-mean deep-intermediate carbon isotope gradient<sup>42</sup>, and  
262 other carbon cycle tracers<sup>39,46</sup>, suggest the vertical gradient of regenerated nutrients and  
263 carbon weakened over deglaciation (Fig. 6b). Finally, records of nutrient utilisation<sup>18</sup> and  
264 export production<sup>4</sup> support an increase in nutrient upwelling to the Southern Ocean's surface  
265 over deglaciation, with boron isotope records<sup>47</sup> demonstrating a concurrent increase in CO<sub>2</sub>  
266 outgassing from the Southern Ocean. The early Holocene maximum in poleward position of  
267 the winds may have led to an overshoot of the oceanic carbon cycle, with enhanced upwelling  
268 and CO<sub>2</sub> outgassing persisting until ~6 ka<sup>4,47</sup>. However, atmospheric CO<sub>2</sub> decreased by ~10  
269 ppm from 10 to 6 ka suggesting uptake by another sink, likely the terrestrial biosphere<sup>48</sup>.

270

271 Our findings indicate that shifts in the Southern Hemisphere westerlies are likely to  
272 have played a key role in driving the deglacial rise in atmospheric CO<sub>2</sub> (ref<sup>33</sup>), and thus may  
273 be an important mechanism underlying glacial-interglacial CO<sub>2</sub> variations<sup>2,3</sup>. Given that  
274 atmospheric CO<sub>2</sub> and global temperature may also influence the latitude of the westerly  
275 winds<sup>8-10</sup>, a deglacial feedback mechanism has been proposed<sup>2</sup>. The apparent temporal lead  
276 of shifts in the westerlies over atmospheric CO<sub>2</sub> and global temperature during certain intervals  
277 of the deglaciation indicated by our reconstruction (Fig 3c) suggests that some initial change  
278 in the winds, perhaps driven by obliquity<sup>18,49</sup>, could have initiated a cascade of increasing CO<sub>2</sub>,  
279 global warming, and poleward shifting winds. The tight coupling demonstrated here between  
280 the latitude of the westerlies and atmospheric CO<sub>2</sub> over the last deglaciation, together with the  
281 sensitivity of the abyssal circulation and carbon cycle to the latitude of the westerlies in our  
282 ocean-sea-ice-carbon model experiments, suggest that future poleward shifts in the position  
283 of the westerly winds<sup>8-10</sup> are likely to drive a positive feedback on anthropogenic warming—  
284 via a decrease in the efficiency of the biological pump and an increase in natural CO<sub>2</sub>  
285 outgassing from the Southern Ocean<sup>50</sup>.

286

## 287 **Acknowledgements**

288 Some of the collaborations in this study were initiated through the PAGES QUIGS workshop  
289 2020. EM received financial support from French-Swedish project on SO VR-349-2012-6278  
290 and CNRS-INSU project INDIEN-SUD. RCJW was funded by NSF Grant AGS-1929775. LM  
291 acknowledges funding from Australian Research Council grant FT180100606. PS was  
292 supported by the Australian Research Council grant FT190100413 and the Australian National  
293 Computing Infrastructure. MH acknowledges funding from Australian Research Council grant  
294 DP210101650. We acknowledge the World Climate Research Programme's Working Group

295 on Coupled Modelling for the coordination of CMIP and thank the climate modelling groups  
296 for producing and making available their model output.

297

### 298 **Author contributions**

299 WRG, EM, LM and CdL designed the study. EM generated the new  $\delta^{18}\text{O}$  data. WRG compiled  
300 the  $\delta^{18}\text{O}$  data and performed the statistical analysis. RCJW and WRG analysed the coupled  
301 climate model output with input from MK. LM and PS conducted the ocean-carbon model  
302 simulations and analysed the output with CdL. MH provided an analysis of deep-to-surface  
303 transport in the modern ocean to aid interpretation. WRG, CdL and LM developed the  
304 interpretation with input from all authors. WRG led the writing of the manuscript. All authors  
305 contributed to the preparation of the manuscript.

306

### 307 **Competing interests**

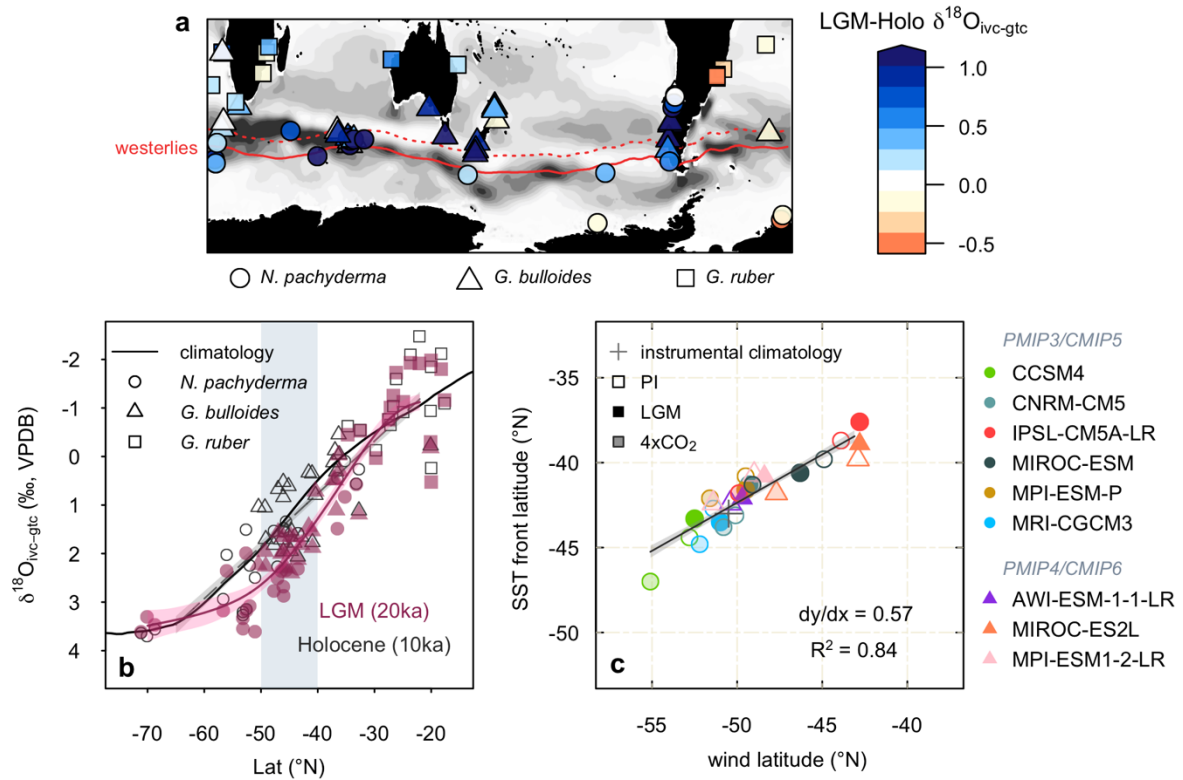
308 The authors declare no competing interests.

309

310 **Correspondence and requests for material** should be addressed to WRG

311

312

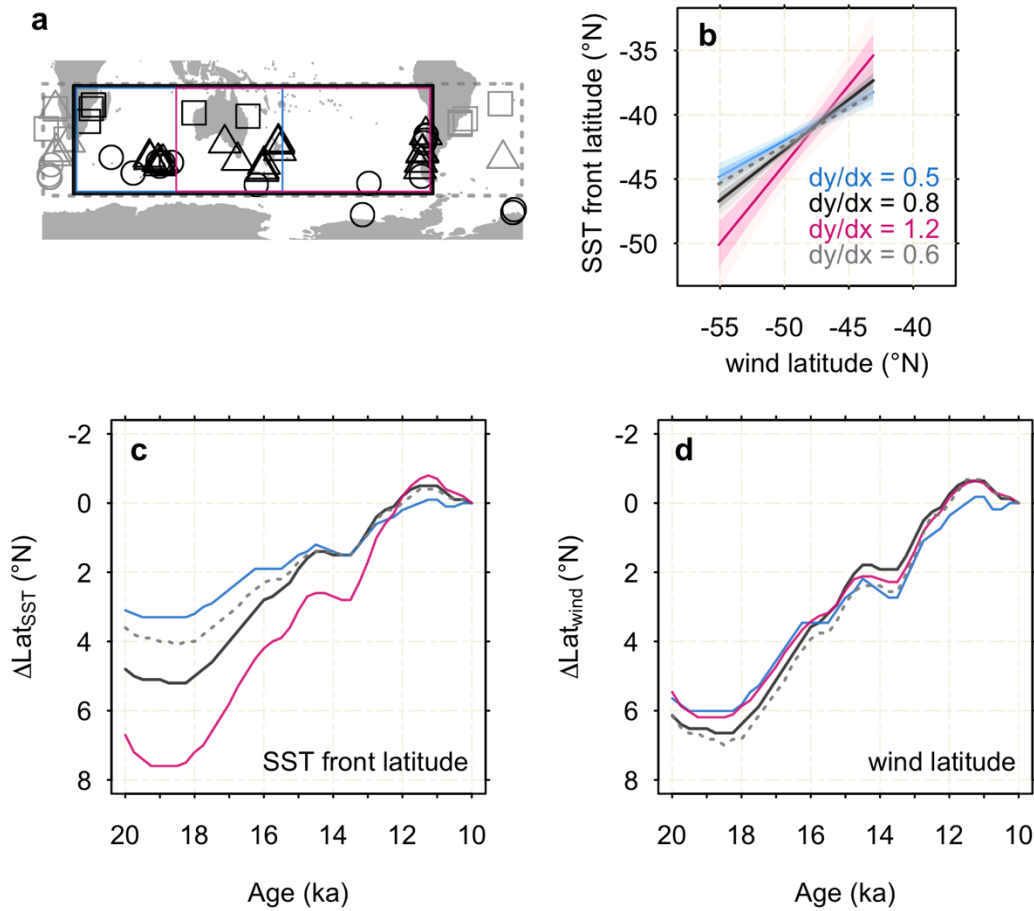


313

314

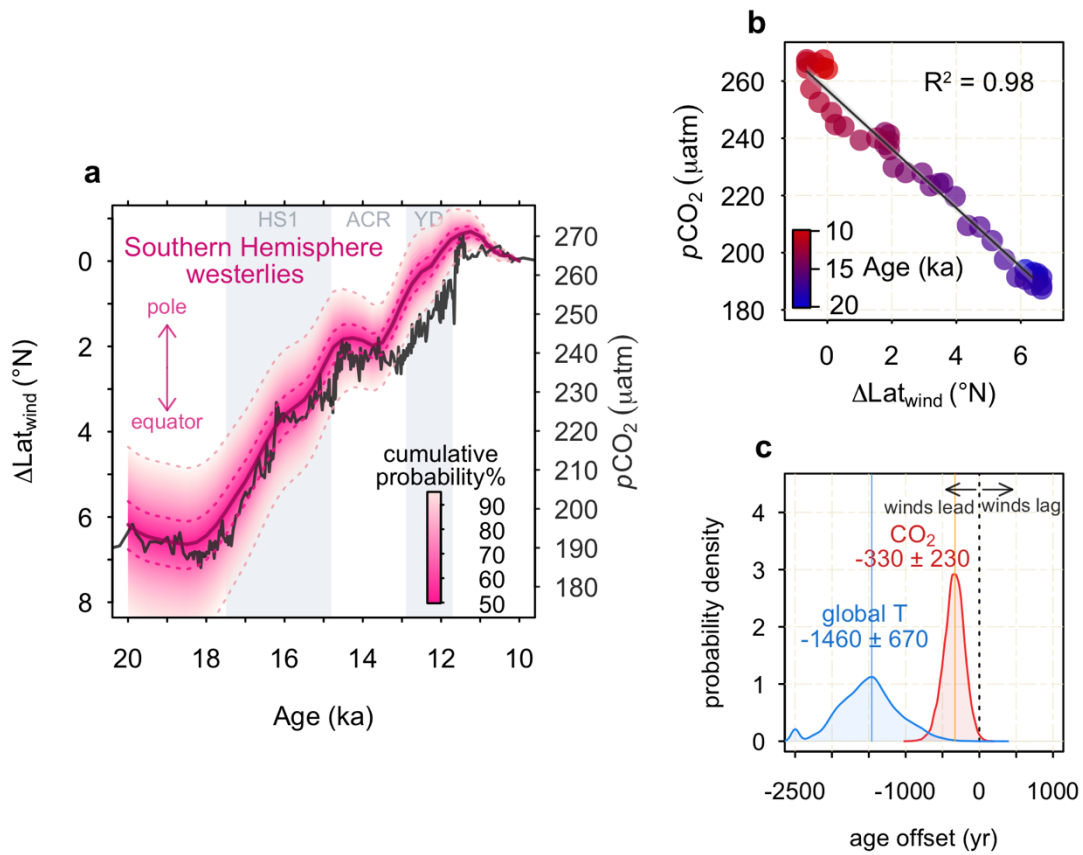
315

316 **Fig. 1:  $\delta^{18}\text{O}$  data and relationship between wind latitude and SST front latitude in the model**  
 317 **ensemble. (a)** LGM-Holocene  $\delta^{18}\text{O}_{\text{ivc-gtc}}$  ( $\delta^{18}\text{O}_{\text{calcite}}$  corrected for ice volume and global-mean SST  
 318 changes; Methods) at the core sites with climatological meridional  $\delta^{18}\text{O}$  gradient represented by  
 319 background shading (Extended Data Fig. 1; darkest shade represents  $0.25\text{‰}/^\circ\text{Lat}$ , equivalent to  $\sim 1$   
 320  $^\circ\text{C}/^\circ\text{Lat}$ ). Modern position of maximum westerlies<sup>51</sup> (solid red line) and the estimated LGM position of  
 321 the westerlies based on a uniform shift (dashed red line). **(b)** LGM and Holocene  $\delta^{18}\text{O}_{\text{ivc-gtc}}$  meridional  
 322 profiles. The grey box shows latitudinal window in which  $\Delta\text{Lat}_{\text{SST}}$  is calculated (Methods). Symbols on  
 323 (a) and (b) distinguish foraminiferal species. **(c)** Relationship between positions of the wind latitude  
 324 (latitude of maximum  $\tau_u$ ) and SST front latitude (latitude of maximum  $\partial\text{SST}/\partial\text{Lat}$ ) within the  
 325 PMIP3/CMIP5 and PMIP4/CMIP6 ensemble (Methods).



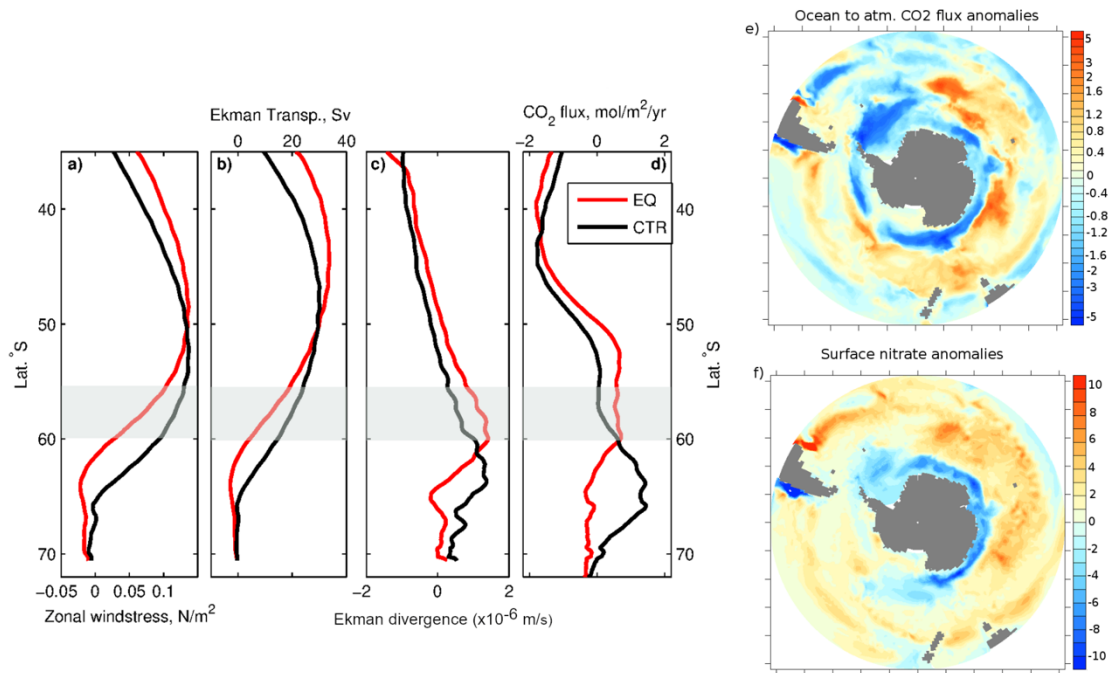
326  
 327  
 328  
 329  
 330  
 331  
 332  
 333  
 334  
 335  
 336

**Fig. 2: SST front and westerly wind changes based on regional subsets** (a) Map showing regional subsets of data. Light grey dashed line corresponds to all core sites. Black includes all Indian-Pacific sites, blue has eastern Pacific sites removed, while pink has western Indian sites removed. Note that given the paucity of data from south of 65°S we include Antarctic marginal sites from all sectors in all regional subsets. (b) Relationship between wind latitude (latitude of maximum zonal-mean  $\tau_u$ ) and regional SST front latitude (latitude of maximum  $\partial\text{SST}/\partial\text{Lat}$ ) within the model ensemble. (c) Reconstructed change in SST front latitude ( $\Delta\text{Lat}_{\text{SST}}$ ) within the regional subsets. (d) Reconstructed zonal-mean wind latitude ( $\Delta\text{Lat}_{\text{wind}}$ ) calculated from the regional  $\Delta\text{Lat}_{\text{SST}}$  reconstruction (c) and the relationships between regional SST front and zonal-mean wind latitude given in (b).



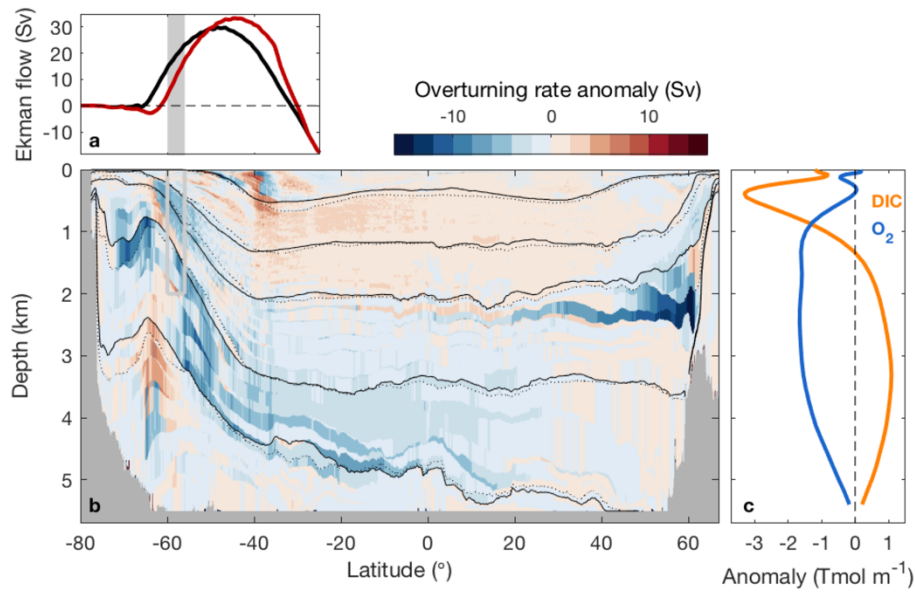
337  
 338  
 339  
 340  
 341  
 342  
 343  
 344

**Fig. 3: Deglacial shifts in the westerlies and atmospheric CO<sub>2</sub>.** (a) Deglacial change in the position of the wind latitude ( $\Delta\text{Lat}_{\text{wind}}$ , lines show the 5<sup>th</sup>, 32<sup>nd</sup>, 50<sup>th</sup>, 68<sup>th</sup>, and 95<sup>th</sup> percentiles) and atmospheric CO<sub>2</sub> (ref<sup>24</sup>) over time. HS1, ACR, and YD are Heinrich Stadial 1, Antarctic Cold Reversal, and Younger-Dryas, respectively. (b) Correlation between  $\Delta\text{Lat}_{\text{wind}}$  and atmospheric CO<sub>2</sub> over deglaciation. (c) Lead-lag between changes in  $\Delta\text{Lat}_{\text{wind}}$  and changes in atmospheric CO<sub>2</sub> and global temperature<sup>31</sup> over deglaciation (Methods).



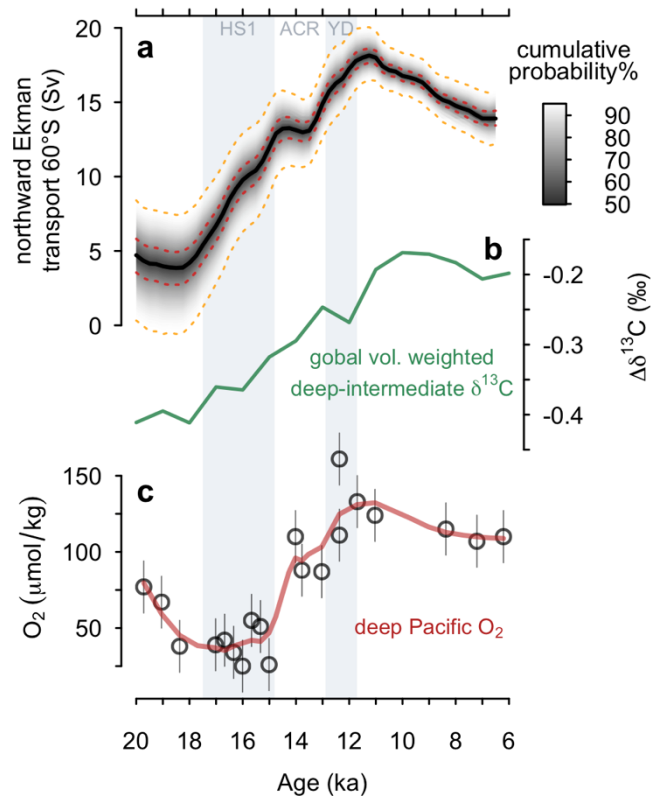
345  
 346  
 347  
 348  
 349  
 350  
 351  
 352  
 353

**Fig. 4: Modelled impact of shifted westerlies on Southern Ocean CO<sub>2</sub> outgassing.** Zonally averaged (a) zonal wind stress, (b) northward Ekman transport, (c) Ekman divergence and, (d) ocean-atmosphere CO<sub>2</sub> flux (positive flux for ocean outgassing). Black curves correspond to the Control equilibrium state (CTR) and red curves to the average over years 116-126 of the Perturbed experiment (EQ). The grey box on (a-d) indicates the latitude of the Drake Passage (56-60°S). 1 Sv is 10<sup>6</sup> m<sup>3</sup> s<sup>-1</sup>. Map of (e) ocean-atmosphere CO<sub>2</sub> flux (mol/m<sup>2</sup>/yr, positive flux for ocean outgassing) and (f) nitrate (mmol/m<sup>3</sup>, average over upper 149 m depth) anomalies, obtained as difference between Perturbed and Control simulations.



354 **Fig. 5: Modelled impact of shifted westerlies on deep ocean circulation and carbon storage. (a)**  
 355 Northward Ekman transport in the Control (Black) and Perturbed (red) simulations. 1 Sv is  $10^6 \text{ m}^3 \text{ s}^{-1}$ .  
 356 **(b)** Global MOC anomaly (Perturbed-Control) after 125 years, normalised for sign such that blue is a  
 357 decrease in overturning rate and red is an increase. Contours show Control (solid) and Perturbed  
 358 (dashed) isopycnals **(c)** Dissolved Inorganic Carbon (DIC) and Oxygen anomalies (Perturbed-Control)  
 359 horizontally integrated globally. Zonally averaged concentration anomalies are shown in Extended Data  
 360 Fig. 10). Grey box on (a) and (b) indicates the Drake Passage.  
 361

362  
363  
364  
365  
366  
367  
368  
369  
370  
371  
372  
373  
374  
375  
376  
377  
378  
379  
380  
381  
382  
383  
384  
385  
386  
387  
388  
389  
390



391  
 392  
 393  
 394  
 395  
 396  
 397  
 398

**Fig. 6: Deglacial changes in northward Ekman transport at 60°S and deep ocean carbon cycling.** (a) Reconstructed change in northward Ekman transport at 60°S over deglaciation (lines show the 5<sup>th</sup>, 32<sup>nd</sup>, 50<sup>th</sup>, 68<sup>th</sup>, and 95<sup>th</sup> percentiles). (b) Global volume-weighted deep-intermediate  $\delta^{13}\text{C}$  gradient<sup>42</sup>, broadly indicative of the vertical gradient in regenerated nutrients/carbon. (c)  $\text{O}_2$  in the deep Pacific<sup>41</sup> (fit with a LOESS smooth), indicative of regenerated carbon storage.

399 **Materials and methods**

400

401 *Planktic foraminiferal  $\delta^{18}\text{O}$  records from the Kerguelen plateau and southeast Pacific*

402 We generated new planktic foraminiferal  $\delta^{18}\text{O}$  data from sediment cores spanning the last  
403 deglaciation located in the mid-latitudes of the Indian and Pacific sectors of the Southern  
404 Ocean. We generated new records from two sediment cores retrieved from the Kerguelen  
405 Plateau during cruise OSCAR INDIEN-SUD (MD12-3396CQ, -47.73 °N, 87.69 °E; MD12-  
406 3401CQ, -44.68°S, 80.39°E). Furthermore, we extended/increased the resolution of two  
407 previously published records from cores located on Kerguelen (MD02-2488, -51.07 °N, 67.73  
408 °E) and in the southeast Pacific (MD07-3119, -46.08 °N, -76.1 °E). We analysed  $\delta^{18}\text{O}$  on either  
409 *G. bulloides* or *N. pachyderma* using a GV Isoprime 100 and an OPTIMA, and a Finnigan  
410 MAT251 and a  $\Delta+$  at CFR/LSCE laboratory. The measurements are reported versus Vienna  
411 Pee Dee Belemnite standard (VPDB) defined with respect to the NBS19 standard. The mean  
412 external reproducibility ( $1\sigma$ ) of carbonate standards is  $\pm 0.06\%$  for  $\delta^{18}\text{O}$ ; the different mass  
413 spectrometers are regularly inter-calibrated and the data are corrected, depending on the  
414 devices, for nonlinearity and the common acid bath. Within this internal calibration, NBS18 is  
415  $-23.2\pm 0.2\%$  VPDB for  $\delta^{18}\text{O}$  and  $-5.0\pm 0.1\%$  VPDB for  $\delta^{13}\text{C}$ . Age models for all the cores are  
416 based on radiocarbon dating, and further details of the age models can be found in ref<sup>52</sup> for  
417 core MD07-3119 and ref<sup>53</sup> for core MD12-3396CQ. Reservoir age changes for the Kerguelen  
418 area followed recent results by ref<sup>53</sup> to establish the age model of core MD12-3401CQ. The  
419 new data are provided in Table S1 and are available on Pangaea (*DOI pending*).

420

421 *Southern Ocean planktic foraminiferal  $\delta^{18}\text{O}$  compilation*

422 We compiled all available existing  $\delta^{18}\text{O}$  records for near-surface dwelling planktic foraminifera  
423 species (*G. ruber*, *G. bulloides*, *N. pachyderma*) spanning the last deglaciation (10-20 ka) from  
424 across the Southern Ocean (refs<sup>54-97</sup>). All records are kept on the original age model of  
425 publication. The compilation contains 64 deglacial records of planktic foraminiferal  $\delta^{18}\text{O}$ . All  
426  $\delta^{18}\text{O}$  data are given in table Table S1 and are available on Pangaea (*DOI pending*).

427

428 *Using planktic foraminiferal  $\delta^{18}\text{O}$  to track the latitude the SST front*

429 Although  $\delta^{18}\text{O}_{\text{calcite}}$  is a function of both temperature and  $\delta^{18}\text{O}_{\text{water}}$ , at the basin scale the effect  
430 of temperature dominates over  $\delta^{18}\text{O}_{\text{water}}$  (Extended Data Fig. 1). Using the Southern Ocean  
431 salinity- $\delta^{18}\text{O}_{\text{water}}$  relationship of ref<sup>98</sup> a meridional salinity difference of greater than 25 PSU  
432 would be required to equal the meridional temperature changes across the basin. As no  
433 physical mechanism exists to drive such changes, the meridional pattern of  $\delta^{18}\text{O}_{\text{calcite}}$  will  
434 always be dominated by temperature, enabling us to use meridional profiles of  $\delta^{18}\text{O}_{\text{calcite}}$  to  
435 identify the latitude of the SST front<sup>19</sup>.

436

437 We quantify changes in the position of the SST front through time ( $\Delta\text{Lat}_{\text{SST}}$ ) from following the  
438 method of ref<sup>19</sup>. Briefly, we first interpolate the  $\delta^{18}\text{O}$  data to 250-year time steps from 20 ka to  
439 10 ka using a Generalised Additive Model (GAM)<sup>99</sup>, with the smoothing term determined by  
440 restricted maximum likelihood (REML)<sup>100</sup>. The reader is referred to ref<sup>101</sup> for an overview of  
441 GAMs. Only foraminiferal  $\delta^{18}\text{O}$  records that span the entire time period of the reconstruction  
442 are utilised such that our analysis is always comparing relative changes in the same cores  
443 through time. The mean resolution of the individual records over deglaciation is about 1 point

444 per 250 yrs and we only include  $\delta^{18}\text{O}_{\text{calcite}}$  records with a minimum of 1 point per 2 ka over the  
445 deglaciation.

446

447 We model the  $\delta^{18}\text{O}$  data at each time step (first correcting for whole ocean effects, see below)  
448 as a function of latitude using a GAM<sup>99</sup>, with the smoothing term determined by restricted  
449 maximum likelihood (REML)<sup>100</sup> (Extended Data Figs. 2 and 3). We compute the shift in latitude  
450 which minimises the Euclidean distance ( $L^2$ ) between the GAM fit at each time step relative to  
451 10 ka, within a  $10^\circ$  latitude band centred around the steepest part of the Holocene meridional  
452 SST/ $\delta^{18}\text{O}_{\text{calcite}}$  profile (-50 to  $-40^\circ\text{N}$ ; grey box in Fig. 1b and Extended Data Figs. 2 and 3). The  
453 10 ka reference time is chosen to maximise the number of records spanning the deglaciation.  
454 Our analysis thus tracks changes in the position of the steepest part of meridional SST profile  
455 across a  $10^\circ$  latitudinal window, rather than the position of any individual front.

456

457 To minimise changes in the meridional  $\delta^{18}\text{O}_{\text{calcite}}$  profile between different time steps that arise  
458 from whole-ocean changes rather than local dynamics we correct the  $\delta^{18}\text{O}_{\text{calcite}}$  data for the  
459 whole ocean change in  $\delta^{18}\text{O}_{\text{water}}$  (arising from ice sheet growth/retreat) and the global-mean  
460 SST change ( $\delta^{18}\text{O}_{\text{ivc-gtc}}$ ). For the whole-ocean change in  $\delta^{18}\text{O}_{\text{water}}$  we scale the LGM-Holocene  
461 change of  $1\pm 0.1\text{‰}$  ( $2\sigma$ ) (ref<sup>102</sup>) to the sea level curve of ref<sup>103</sup>. For the global-mean SST  
462 change we scale the  $-1.7\pm 1.0^\circ\text{C}$  ( $2\sigma$ ) area-weighted global-mean LGM-preindustrial change  
463 in SST from the PMIP3/4 ensemble (see below) to the global temperature record of ref<sup>31</sup>, using  
464 the water-calcite temperature fractionation ( $\delta^{18}\text{O}_{\text{calcite-water}}$ ) of ref<sup>104</sup>, which agrees well with the  
465 pooled-foraminiferal species sensitivity of ref<sup>105</sup>. We propagate all of the uncertainty from these  
466 whole-ocean corrections through to our final results (see below). We note these whole-ocean  
467 corrections make the reconstructed changes in the position of the winds more conservative;  
468 removing the global-mean SST change correction entirely results in an Indian-Pacific  $\Delta\text{Lat}_{\text{SST}}$   
469 of  $\sim 7^\circ$  between 10-20 ka (c.f.  $\sim 5^\circ$  including the correction). Furthermore, our leave-one-out  
470 analysis shows that our reconstruction is primarily driven by mid-latitude sites, indicating these  
471 whole ocean corrections are unlikely to be biasing our results.

472

473 We derive uncertainties via bootstrapping<sup>106</sup> (10,000 iterations), accounting for the age and  
474 analytical uncertainties on individual records as well as the uncertainties in the whole-ocean  
475 change in  $\delta^{18}\text{O}_{\text{water}}$  and the global-mean SST change with Monte-Carlo simulation. We ascribe  
476 conservative age uncertainties of  $\pm 1000$  years ( $2\sigma$ ), and analytical uncertainties of  $\pm 0.08\text{‰}$   
477 ( $2\sigma$ ) to all planktic foraminiferal  $\delta^{18}\text{O}$  records. The R code and data used to perform the  
478 analysis is provided on Github (<https://github.com/willyrgray/SOd18O>).

479

480 We repeat the analysis over a longer time period (22-6.5 ka) which necessitates using a  
481 smaller subsection of cores and thus results in larger uncertainties (Extended Data Fig. 6).  
482 Still, the results show excellent agreement with the complete set of cores (i.e. spanning 10-20  
483 ka) (Extended Data Fig. 6), with a ratio of 0.95 during the overlapping interval. We apply this  
484 correction to the longer reconstruction, though the correction makes a negligible difference  
485 and does not impact our conclusions (Extended Data Fig. 6). Performing the analysis further  
486 into the Holocene (22-2.5 ka) results in substantially higher uncertainties due to the lack of  
487 cores spanning this interval, but the results suggest the westerlies are relatively stable through  
488 the late Holocene (Extended Data Fig. 6), in agreement with qualitative indicators of the  
489 winds<sup>23,107</sup>.

490

491 *Leave-one-out analysis*

492 We perform a jackknife resampling of the dataset to determine the contribution of each planktic  
493 foraminiferal  $\delta^{18}\text{O}$  record to the Indian-Pacific  $\Delta\text{Lat}_{\text{SST}}$  reconstruction. We sequentially remove  
494 each record from the dataset, recompute  $\Delta\text{Lat}_{\text{SST}}$ , and determine the contribution of that record  
495 as the time-integrated absolute difference from  $\Delta\text{Lat}_{\text{SST}}$  computed using the entire dataset  
496 (expressed as a percentage of the absolute cumulative change in  $\Delta\text{Lat}_{\text{SST}}$  over deglaciation;  
497 Extended Data Fig. 4). This analysis shows that no single record is contributing more than 5%  
498 of the total signal, and that the cores with the highest weighting are all located in the mid-  
499 latitudes. Thus, we conclude that our reconstruction is primarily tracking a mid-latitude signal.

500

501 *Seasonality of planktic foraminifera*

502 Our approach assumes that any changes in the seasonal bias of foraminifera relating to their  
503 habitat preference are small relative to the change in temperature due to the movement of the  
504 SST front. The validity of this approach is supported by  $\delta^{18}\text{O}$  records measured on species of  
505 foraminifera with different temperature/seasonal habitats at the same (or nearby) mid-latitude  
506 sites within the compilation. Foraminiferal species with different habitat temperature (and thus  
507 seasonal) preferences (*G. bulloides* and *N. pachyderma*, ref <sup>108</sup>) show very similar Holocene-  
508 LGM changes (compare circles and triangles on Fig. 1a). Furthermore, the leave-one-out  
509 analysis (Extended Data Fig. 4) shows that records of *G. bulloides* and *N. pachyderma*  $\delta^{18}\text{O}$   
510 (which should have different seasonal biases) are both contributing highly to the  $\Delta\text{Lat}_{\text{SST}}$   
511 reconstruction. This suggests the impacts of seasonality on the reconstruction are likely to be  
512 small. Crucially, the relatively warm temperature preference of *G. bulloides* (the dominant  
513 species in the mid-latitudes) means that global SST cooling during the LGM would shift the  
514 annual SST distribution further away from its preferred habitat temperature, shifting its  
515 seasonal bias further towards the summer and minimising the degree of glacial cooling it  
516 records. This would thus make the anomalous mid-latitude cooling we see in the LGM more  
517 conservative relative to the annual mean cooling, thus making our reconstruction of changes  
518 in the wind latitude more conservative.

519

520 *PMIP3/4 and CMIP5/6 ensemble*

521 We use an ensemble of models from the Paleoclimate Modelling Intercomparison Project  
522 (PMIP3<sup>109</sup> and PMIP4<sup>20,110</sup>) and Coupled Model Intercomparison Project (CMIP5<sup>111</sup> and  
523 CMIP6<sup>112</sup>); data available at <https://esgf-node.llnl.gov/projects/esgf-llnl/>. We use all  
524 CMIP5/PMIP3 and CMIP6/PMIP4 models for which both SST and zonal surface wind fields  
525 are available for the LGM and preindustrial simulations, and also include the 4xCO<sub>2</sub>  
526 simulations from these models where available. Annual-mean climatologies are calculated  
527 from the final 100 years of each simulation and interpolated to a common 2-degree analysis  
528 grid.

529

530 To convert the reconstructed changes in the SST front latitude ( $\Delta\text{Lat}_{\text{SST}}$ ) to changes in the  
531 latitude of the westerly winds we use the relationship between the SST front latitude and the  
532 wind latitude within the ensemble. We calculate the SST front latitude as the latitude of  
533 maximum meridional SST gradient ( $\partial\text{SST}/\partial\text{Lat}$ ) in each simulation within a 10° latitudinal  
534 averaging window (to emulate the 10° latitudinal window used to calculate  $\Delta\text{Lat}_{\text{SST}}$  from the  
535  $\delta^{18}\text{O}_{\text{ivc-gtc}}$  data downcore. We do this using zonal-mean SST across the Southern Ocean (Fig.  
536 1c) and across regional subsets (Fig. 2; Extended Data Fig. 5). We calculate the wind latitude  
537 as the latitude of maximum zonal-mean zonal wind stress ( $\tau_u$ ). We regress the SST front

538 latitude against wind latitude (Fig. 2; Extended Data Fig. 5) and then apply this relationship to  
539 our  $\Delta\text{Lat}_{\text{SST}}$  reconstruction in order to determine changes in the position of the wind latitude  
540 ( $\Delta\text{Lat}_{\text{wind}}$ ), propagating the uncertainty in the relationship through to our final estimates of  
541  $\Delta\text{Lat}_{\text{wind}}$  using Monte-Carlo simulation. We exclude the MPI model from the regressions for the  
542 Indian-Pacific sector, as this model sits as an outlier from the remainder of the ensemble  
543 (however we note the slope between wind latitude and SST front latitude within the MPI model  
544 is consistent with the rest of the ensemble). The peculiarity of the MPI model is possibly due  
545 to SST biases relating to meridional heat transport in the Indian sector within the model<sup>113</sup>,  
546 where we find the largest difference relative to the other models. Including the MPI model in  
547 the Indian-Pacific sector regression has a negligible effect on our results, slightly increasing  
548 the reconstructed change in the wind latitude ( $\Delta\text{Lat}_{\text{wind}}$ ) between 10-20 ka from 6.2° to 6.7°  
549 and increasing the uncertainty by 0.5° at the 95% CI. The  $\Delta\text{Lat}_{\text{wind}}$  reconstruction is provided  
550 in Table S2.

551

### 552 *Regional subset test*

553 To ascertain that our method is able to track zonal-mean shifts in the wind latitude from  
554 changes in the SST front latitude (which is also affected by bathymetry and ocean  
555 eddies<sup>25,28,114</sup>), we perform a regional subset test. We sequentially remove regional subsets of  
556 cores from the compilation, re-compute  $\Delta\text{Lat}_{\text{SST}}$ , and recalculate the relationship between the  
557 zonal-mean wind latitude and the regional SST front latitude (Fig. 2). The results demonstrate  
558 that the difference in zonal-mean  $\Delta\text{Lat}_{\text{wind}}$  reconstructed from the regional subsets is markedly  
559 smaller than the difference in  $\Delta\text{Lat}_{\text{SST}}$  between the regional subsets. This indicates that (i) the  
560 model ensemble and (ii) our method to track the SST front downcore, capture the regional  
561 SST front response to zonal-mean shifts in the wind latitude. We can thus confidently apply  
562 the relationship observed in the model ensemble to estimate shifts in the zonal-mean latitude  
563 of the westerlies using the Indian-Pacific  $\Delta\text{Lat}_{\text{SST}}$  reconstruction over deglaciation.

564

### 565 *Reconstructing peak wind stress*

566 Using our  $\Delta\text{Lat}_{\text{wind}}$  reconstruction and the relationship between wind latitude and the  
567 magnitude of peak wind stress in the model ensemble (*wind strength*, Extended Data Fig. 5),  
568 we estimate changes in the magnitude of peak wind stress over deglaciation (Extended Data  
569 Fig. 8). The tendency for the magnitude of peak wind stress to decrease as the winds move  
570 equatorward (and vice-versa) has been previously noted<sup>115,116</sup>. Our reconstructed equatorial  
571 shift in the wind latitude implies a weakening of the peak westerlies by 0.034 N m<sup>-2</sup> (about  
572 25%) during the LGM relative to the mid Holocene, resulting in a LGM wind strength of 0.106  
573 (0.085-0.12, 95% CI) N m<sup>-2</sup>, assuming mid-Holocene wind stress is equal to the modern  
574 climatology (0.14 N m<sup>-2</sup>; Fig. 4a). This assumption is supported by qualitative tracers of the  
575 westerlies<sup>23,107</sup> which indicate little change between ~6.5 ka and the present day.  
576 Furthermore, running our analysis further into the Holocene suggests little change in the  
577 position of the winds (Extended Data Fig. 6), although uncertainties are very large given the  
578 few core sites that span this interval. Although the shape of the zonal-mean westerly wind  
579 profile may have changed together with the latitude and magnitude of its peak, the model  
580 ensemble suggests that the meridional wind profile changes little between PI and LGM  
581 states; there is a -0.25±7% and 0.5±3.5% ensemble mean change in peak width at 50% and  
582 15% peak height, respectively, between LGM and preindustrial. Furthermore, we observe no  
583 significant relationship between the wind latitude and the peak width (at either 50% or 15%  
584 peak height) within the ensemble, such that we do not expect substantial changes in the

585 shape of the wind profile as the winds shift. The wind strength (max  $\tau_u$ ) reconstruction is  
586 provided in Table S2.

587

#### 588 *Reconstructing northward Ekman transport at 60°S*

589 To calculate changes in zonal wind stress at 60°S (60S  $\tau_u$ ) we use the relationship between  
590 the wind latitude and the zonal-mean zonal wind stress at 60°S in the model ensemble  
591 (Extended Data Fig. 5d), and apply this relationship to our reconstruction of  $\Delta\text{Lat}_{\text{wind}}$ ,  
592 propagating through the uncertainty in the relationship (Extended Data Fig. 8). We assume  
593 mid-Holocene wind stress equal to the modern climatology (0.09 N m<sup>-2</sup>; Fig. 4a). We calculate  
594 northward Ekman transport (Fig. 6a) as the zonal integral of  $\tau_u/(\rho_0 * f)$ , where  $\rho_0$  is the density  
595 of seawater (1027 kg/m<sup>3</sup>) and  $f$  is the Coriolis parameter. The reconstruction of 60S  $\tau_u$  and  
596 northward Ekman transport at 60°S is provided in Table S2. The ensemble shows that the  
597 latitude of the peak in zonal wind stress is a better predictor of wind stress at 60°S ( $R^2= 0.9$ ;  
598 Extended Data Fig. 5d) than the magnitude of the peak in wind stress ( $R^2= 0.7$ ).

599

#### 600 *Lead-lag analysis*

601 We calculate the lead-lag between the Indian-Pacific  $\Delta\text{Lat}_{\text{SST}}$  reconstruction and the change  
602 in atmospheric CO<sub>2</sub> (or in global temperature) over deglaciation as the time offset that  
603 maximises the correlation between the two time series, broadly following the approach of ref<sup>31</sup>.  
604 We account for age uncertainties in the CO<sub>2</sub> record using the typical gas age uncertainty in  
605 the WAIS divide ice core over deglaciation<sup>117</sup> ( $\pm 75$  yrs,  $1\sigma$ ). For the age uncertainty in the  
606 global mean temperature stack we take the uncertainty in the lag of global temperature over  
607 CO<sub>2</sub> ( $\pm 340$  yrs,  $1\sigma$ ) in ref<sup>31</sup>. To account for age uncertainties in the Indian-Pacific  $\Delta\text{Lat}_{\text{SST}}$   
608 reconstruction we repeat the lead-lag analysis using each boot strap/Monte-Carlo iteration of  
609 the Indian-Pacific  $\Delta\text{Lat}_{\text{SST}}$  reconstruction. This approach assumes age uncertainties within the  
610  $\delta^{18}\text{O}$  compilation are uncorrelated, which is unlikely to strictly hold given e.g. reservoir age  
611 changes (although methodological differences between studies add a source of random  
612 'human behavioural' error), but provides a first-order assessment of leads and lags between  
613 the different time series. As a sensitivity test, we repeat the lead-lag analysis with CO<sub>2</sub>,  
614 including varying degrees of 'structural' uncertainty in the Indian-Pacific  $\Delta\text{Lat}_{\text{SST}}$   
615 reconstruction. This suggests that the lead in the change in the winds over CO<sub>2</sub> is significant  
616 at the 95% level until more than ~30% of the age uncertainty is correlated across the  
617 compilation. Assuming 100% of the age uncertainty is correlated (i.e. perfect covariance)  
618 results in uncertainties of  $\pm 860$  yrs (95% CI). To test whether the lead of  $\Delta\text{Lat}_{\text{SST}}$  relative to  
619 CO<sub>2</sub> holds in the early deglaciation, we repeat this analysis for 20-14 ka (cf. 20-10 ka) and find  
620 a lead of 160 yrs (-10 to 330 yrs 95% CI), cf. 330 yrs (100 to 560 yrs 95% CI).

621

#### 622 *Experiments with a 0.25° ocean-sea-ice-carbon model*

623 We use the ocean-sea-ice-carbon model MOM5-SIS-Wombat with a Mercator horizontal  
624 resolution of 0.25° (~11 km grid spacing at 65°S), and 50 vertical levels<sup>33,34</sup>. The model is  
625 initialised with modern-day temperature and salinity distributions, and biophysical fields  
626 derived from an observation-based climatology (GLODAP v2, 2016)<sup>118</sup>. The model is then  
627 spun-up for 700 years with version 2 of the Coordinated Ocean-ice Reference Experiments  
628 (CORE) Normal Year Forcing (NYF) reanalysis data<sup>119</sup>, representative of a 'normal year'  
629 during the recent instrumental period. To study the impact of equatorward shifted southern  
630 hemispheric westerlies, a 4° equatorward shift (with no change in magnitude) is applied to the  
631 near surface wind speeds between 25°S and 70°S. The perturbation simulation is run for 125

632 years. Given the carbon and nutrient cycles have around an order of magnitude longer time  
633 scales in the deep Pacific<sup>17</sup>, the perturbation simulation is far from equilibrium, but it does  
634 provide a strong indication of the impact on circulation and the carbon cycle. Anomalies are  
635 calculated as the difference, averaged over the last 10 years, between the Perturbed  
636 experiment and the concomitantly extended Control experiment to remove the influence of  
637 linear model drift.

638

639 The model includes a parameterization for the effects of mesoscale eddies, with isopycnal  
640 tracer<sup>120</sup> and thickness<sup>121</sup> diffusivities set to  $600 \text{ m}^2 \text{ s}^{-1}$ . The meridional overturning circulation  
641 (Fig. 5b and Extended Data Fig. 9) includes both resolved and parameterized advection. It is  
642 calculated in neutral density<sup>122</sup> coordinate and reprojected onto the depth coordinate<sup>123</sup> in  
643 order to eliminate adiabatic recirculations and avoid spurious effects due to vertical inversions  
644 in potential density fields.

645

646 As a result of the equatorward shifted winds, the Ekman pumping is suppressed south of  $60^\circ\text{S}$ ,  
647 and the ACC weakens by 6% (122 Sv instead of 130 Sv). South of  $60^\circ\text{S}$ , the surface DIC  
648 concentration decreases by  $13 \text{ mmol/m}^3$  (Extended Data Fig. 10), thus leading to a surface  
649  $p\text{CO}_{2\text{DIC}}$  decrease of 25 ppm, which is partly compensated by a decrease of surface alkalinity  
650 of  $8.6 \text{ mmol/m}^3$  ( $\Delta p\text{CO}_{2\text{alk}} = +14 \text{ ppm}$ ). A small decrease in surface salinity is  
651 compensated by a small increase in SST, so that the solubility contribution to  $p\text{CO}_{2\text{sol}}$  is  
652 negligible south of  $60^\circ\text{S}$ . As a result, the  $\text{CO}_2$  outgassing over the polar Southern Ocean (south  
653 of  $60^\circ\text{S}$ ) is completely suppressed (Fig. 4d). On the other hand, the equatorward shift in the  
654 westerlies and associated increased Ekman pumping north of  $60^\circ\text{S}$  leads to a greater  $\text{CO}_2$   
655 outgassing in that region. Nevertheless, if integrated over the Southern Ocean (south of  $35^\circ\text{S}$ ),  
656 there is an anomalous uptake of 27 GtC by the Southern Ocean over the course of the  
657 Perturbed experiment, equivalent to a  $\text{CO}_2$  decrease of 13 ppm. While the model also displays  
658 an increase in Southern Ocean sea ice extent in the Perturbed experiment (not shown), likely  
659 an impact of the reduction in upwelling of relatively warm deepwaters, the decrease in  $\text{CO}_2$   
660 flux out of the polar ocean is associated with decreased surface ocean  $p\text{CO}_2$  rather than  
661 increased air-sea disequilibria. Hence, changes in wind-driven carbon supply, rather than sea  
662 ice driven disequilibria, cause the reduction in  $\text{CO}_2$  outgassing from the polar Southern Ocean.  
663 Furthermore, the  $\text{CO}_2$  flux anomalies are largely decoupled from the sea ice anomalies around  
664 the basin. Both  $p\text{CO}_2$  and  $\text{CO}_2$  flux anomalies are, however, clearly linked to changes in  
665 Ekman divergence.

666

667 As a result of shifted winds, the strength of the lower overturning cell (maximum stream flow  
668 below 2500 m within  $20\text{-}50^\circ\text{S}$ ) weakens by 3 Sv, from 16 to 13 Sv and the mixed layer shoals  
669 in the polar Southern Ocean (Fig. 5b; Extended Data Fig. 9). The DIC concentration increases  
670 in the Southern Ocean below the sub-surface south of  $60^\circ\text{S}$  by about  $10 \text{ mmol/m}^3$ , and the  
671 slowdown of the lower cell causes DIC to increase throughout the deep ocean below 1.5km  
672 (Fig. 5c; Extended Data Fig. 10), even if the magnitude of the increase is small due to the  
673 short duration of the experiment. The increase in upwelling between  $60^\circ\text{S}$  and  $50^\circ\text{S}$  leads to  
674 a DIC increase in the upper 2000m depth in that region, but causes the overturning of the  
675 upper cell to increase by 6.4 SV (maximum overturning between 500-1000m and  $20^\circ\text{S}\text{-}40^\circ\text{S}$ ;  
676 Fig. 5b; Extended Data Fig. 9) which results in a DIC decrease in the intermediate depths  
677 throughout the ocean north of  $35^\circ\text{S}$  (Fig. 5c; Extended Data Fig. 10). These DIC changes are  
678 accompanied by similar changes in remineralised nitrogen, and inverse changes in dissolved  
679  $\text{O}_2$ , highlighting the role of changes in oceanic circulation.

680

681 The reduction in upwelling within the polar Southern Ocean causes the preformed nitrate  
682 concentration of Antarctic Bottom Water to decrease. This may be enhanced by a shoaling of  
683 the polar Southern Ocean mixed layer depth within the simulation (Extended Data Fig. 9),  
684 which would reduce light limitation, providing a potential mechanism to further increase the  
685 utilisation of the upwelled nutrients<sup>13</sup>. Driven by a reduction in water column mixing due to a  
686 shoaling of the mixed layer in deepwater formation regions of the North Atlantic (not shown),  
687 the preformed nitrate concentration of the northern end member also decreases. As such, the  
688 preformed nitrate concentration begins to decrease throughout the deep ocean, with a 1.3%  
689 increase in global mean  $N^*$  ( $N^*$  = regenerated  $\text{NO}_3$ /total  $\text{NO}_3$ ) after 125 years (Extended Data  
690 Fig. 10). The short duration of the Perturbed experiment inhibits a full quantification of the  $\text{CO}_2$   
691 response. However, by extrapolating the initial changes in endmember preformed  $\text{NO}_3$  ( $N_{\text{pre}}$ ,  
692 given in  $\text{mmol/m}^3$ ) based on the relative volume of the ocean they represent ( $V$ ) we can broadly  
693 estimate the magnitude of  $\text{CO}_2$  change implicated by the initial changes in endmember  
694 preformed nitrate.

695

696 We take the Southern Ocean endmember as an average through the water column between  
697  $60\text{-}80^\circ\text{S}$ , and the North Atlantic endmember as an average through the water column between  
698  $60\text{-}70^\circ\text{N}$  in the North Atlantic. In the control run  $N_{\text{pre\_SO\_ctr}} = 22.12$  and  $N_{\text{pre\_NA\_ctr}} = 8.5$ .  
699 Global mean  $N_{\text{pre}}$  in the control run ( $N_{\text{pre\_ctr}}$ ) is 15.45. Using the global mean and endmember  
700 values we calculate the volumetric contribution of the Southern Ocean endmember ( $V_{\text{SO}}$ ) as  
701 0.51 and the North Atlantic endmember ( $V_{\text{NA}}$ ) as 0.49. Total nitrate ( $N_{\text{tot}}$ ) is  $33.84 \text{ mmol/m}^3$   
702 such that globally averaged  $N^*$  in the control run is 54%.

703 After 125 years of the Perturbed experiment  $N_{\text{pre}}$  in both the endmembers decreases:  
704  $N_{\text{pre\_SO\_125}} = 20.31$  and  $N_{\text{pre\_NA\_125}} = 7.3$ . Assuming the same volumetric contributions  
705 as the control experiment, we calculate the expected change in global mean  $N_{\text{pre}}$  in the  
706 Perturbed run ( $N_{\text{pre\_EQSH}}$ ) as,  
707  $N_{\text{pre\_EQSH}} = V_{\text{SO}} * N_{\text{pre\_SO\_125}} + V_{\text{NA}} * N_{\text{pre\_NA\_125}} = 13.9$ , equivalent to a globally averaged  
708  $N^*$  value of 59%.

709

710 Based on the initial changes in  $N_{\text{pre}}$  within the endmember regions we would thus expect a  
711 global mean  $N^*$  increase of ~5% in the Perturbed experiment relative to the Control, once  
712 these anomalies had propagated through the deep ocean. Applying the sensitivity of  
713 atmospheric  $\text{CO}_2$  to global preformed nutrients of ref<sup>15</sup>, this increase in  $N^*$  within the Perturbed  
714 experiment equates to an atmospheric  $\text{CO}_2$  decrease of ~15 ppm. However, timeseries of the  
715 endmember  $N_{\text{pre}}$  values indicate they are not yet equilibrated and are still decreasing after 125  
716 years such that this likely represents a conservative estimate of the increase  $N^*$  and  
717 associated lowering of  $\text{CO}_2$  we would expect if the Perturbed experiment was run to  
718 equilibrium.

719

720 Further to this effect, the model indicates a redistribution of the regenerated nutrient and  
721 carbon pools from the intermediate depths toward the abyss. The deepening of the  
722 regenerated nutrient and carbon pools would drive a further  $\text{CO}_2$  decrease via carbonate  
723 compensation<sup>16,37</sup>. The higher DIC content at depth would lower the carbonate ion  
724 concentration, increasing  $\text{CaCO}_3$  dissolution within the ocean. This in turn would result in a  
725 transient increase in alkalinity, lowering atmospheric  $\text{CO}_2$ . While the scaling between  
726 preformed nutrients and atmospheric  $\text{CO}_2$  used above (ref<sup>37,124</sup>) accounts for a linear  
727 approximation of  $\text{CaCO}_3$  dissolution following the total increase in regenerated carbon within

728 the ocean, the effect of nutrient deepening is not accounted for by this scaling. Based on the  
729 initial changes we see in deep ocean DIC in the model (Extended Data Fig. 10), and the  
730 scaling between intermediate-deep DIC and atmospheric CO<sub>2</sub> given in given refs<sup>37,124</sup> we  
731 would thus expect a further substantial decrease in CO<sub>2</sub>.

732

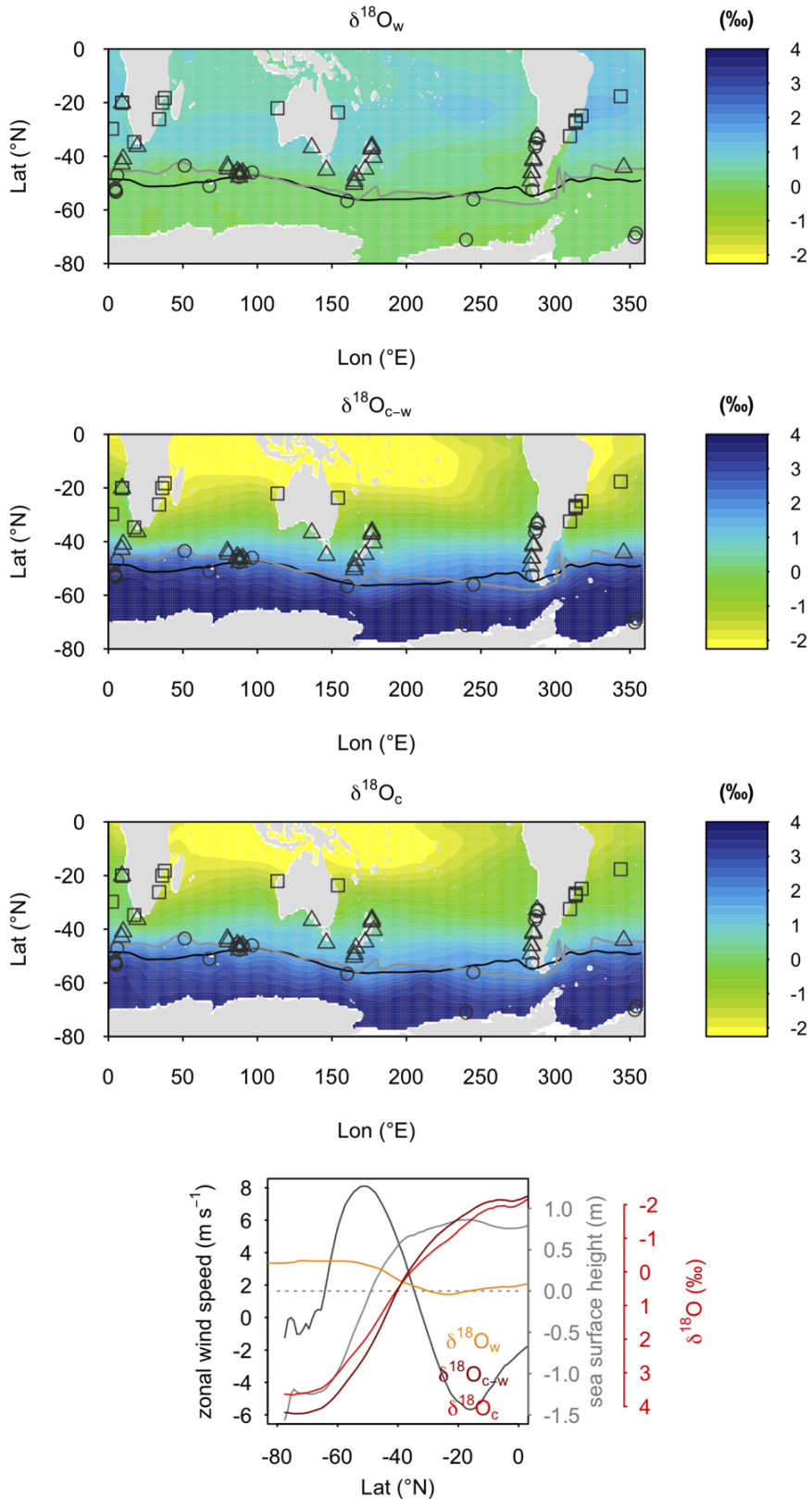
#### 733 **Data availability**

734 The new and compiled  $\delta^{18}\text{O}$  data are given in table Table S1 and are available on Pangaea  
735 (*DOI pending*). The westerly wind reconstructions generated in this study are given in table  
736 Table S2. The PMIP and CMIP data are available from <https://esgf-node.llnl.gov/projects/esgf-llnl/>.

738

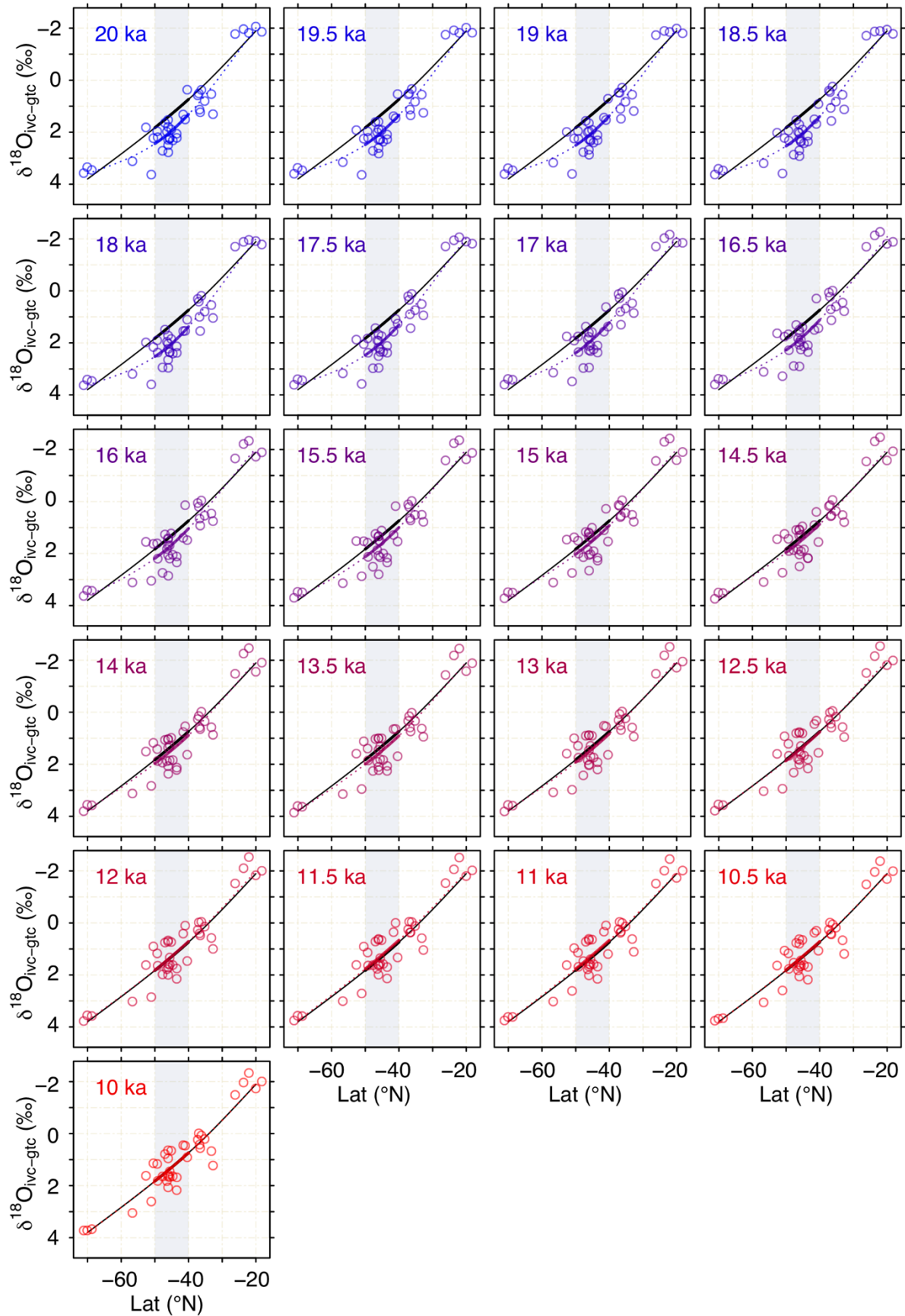
#### 739 **Code availability**

740 The R code and data used to perform the  $\Delta\text{Lat}_{\text{SST}}$  analysis is provided on Github  
741 (<https://github.com/willyrgray/SOd18O>).



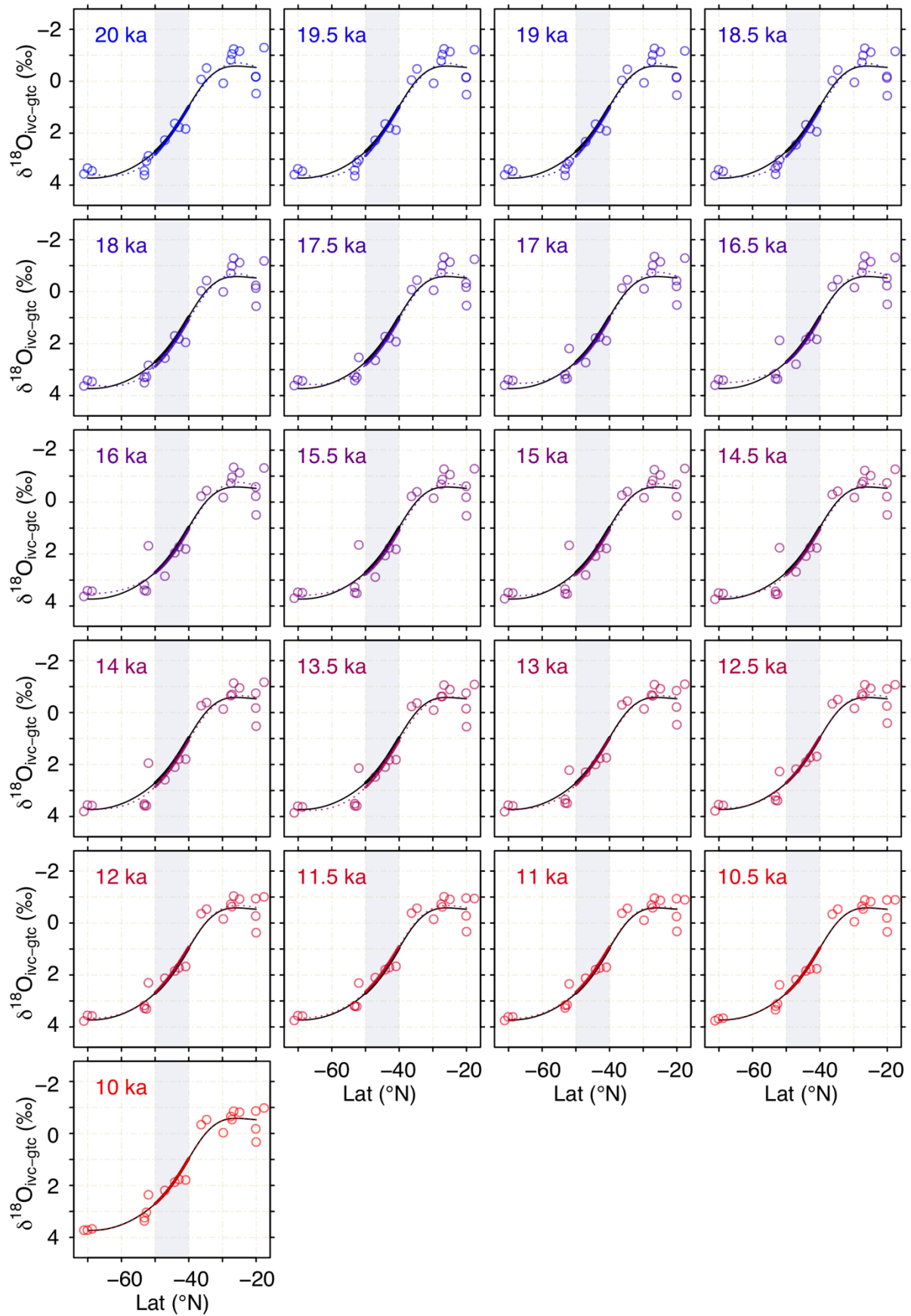
742

743 **Extended Data 1. Climatological  $\delta^{18}\text{O}$ .** Climatological  $\delta^{18}\text{O}_{\text{water}}$  (ref<sup>98</sup>),  $\delta^{18}\text{O}_{\text{calcite-water}}$  (calculated using  
 744 refs<sup>104,125</sup>), and  $\delta^{18}\text{O}_{\text{calcite}}$  (note, colour scale is the same for panels). Symbols show location of core  
 745 sites and species of planktic foraminifera (circles = *N. pachyderma*, triangles = *G. bulloides*, squares =  
 746 *G. ruber*). Black line shows the position of westerlies as determined by maximum zonal wind speed  
 747 (ref<sup>51</sup>) and grey line shows zero sea surface height anomaly ref<sup>126</sup>). Zonal-mean climatological  
 748  $\delta^{18}\text{O}_{\text{water}}$ ,  $\delta^{18}\text{O}_{\text{calcite-water}}$ , and  $\delta^{18}\text{O}_{\text{calcite}}$  (as shown on Fig. 1), zonal wind speed, and sea surface height.



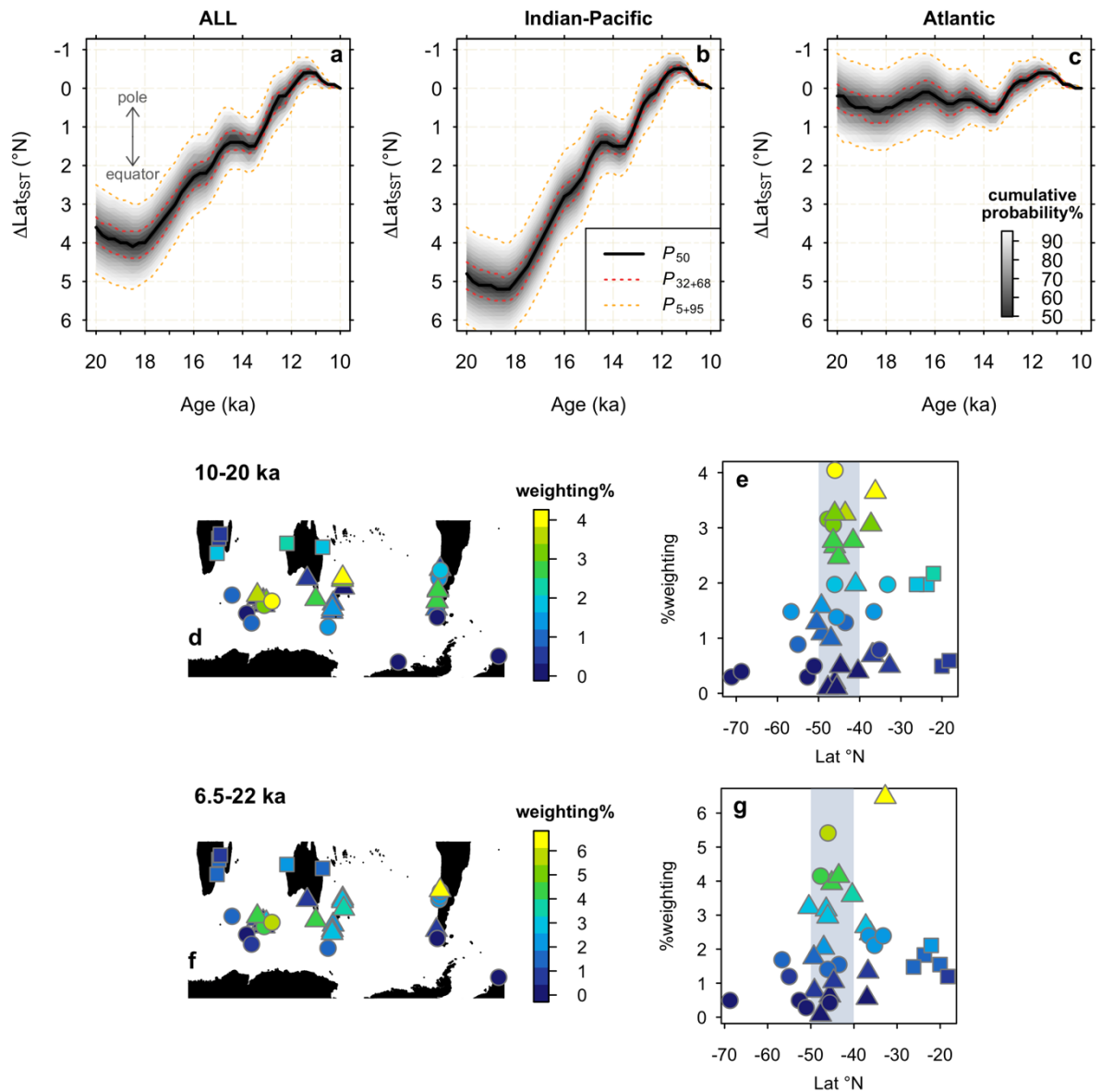
749  
750  
751  
752

**Extended Data 2. Indian-Pacific meridional  $\delta^{18}\text{O}$  profiles.** Indian-Pacific meridional  $\delta^{18}\text{O}_{\text{IVC-gtc}}$  data with GAM fits at 500-year time steps. The GAM fit at 10 ka is shown in black. The grey box is the window in which  $\Delta\text{Lat}_{\text{SST}}$  is calculated and the thick lines show the portion of the curves falling within this window.

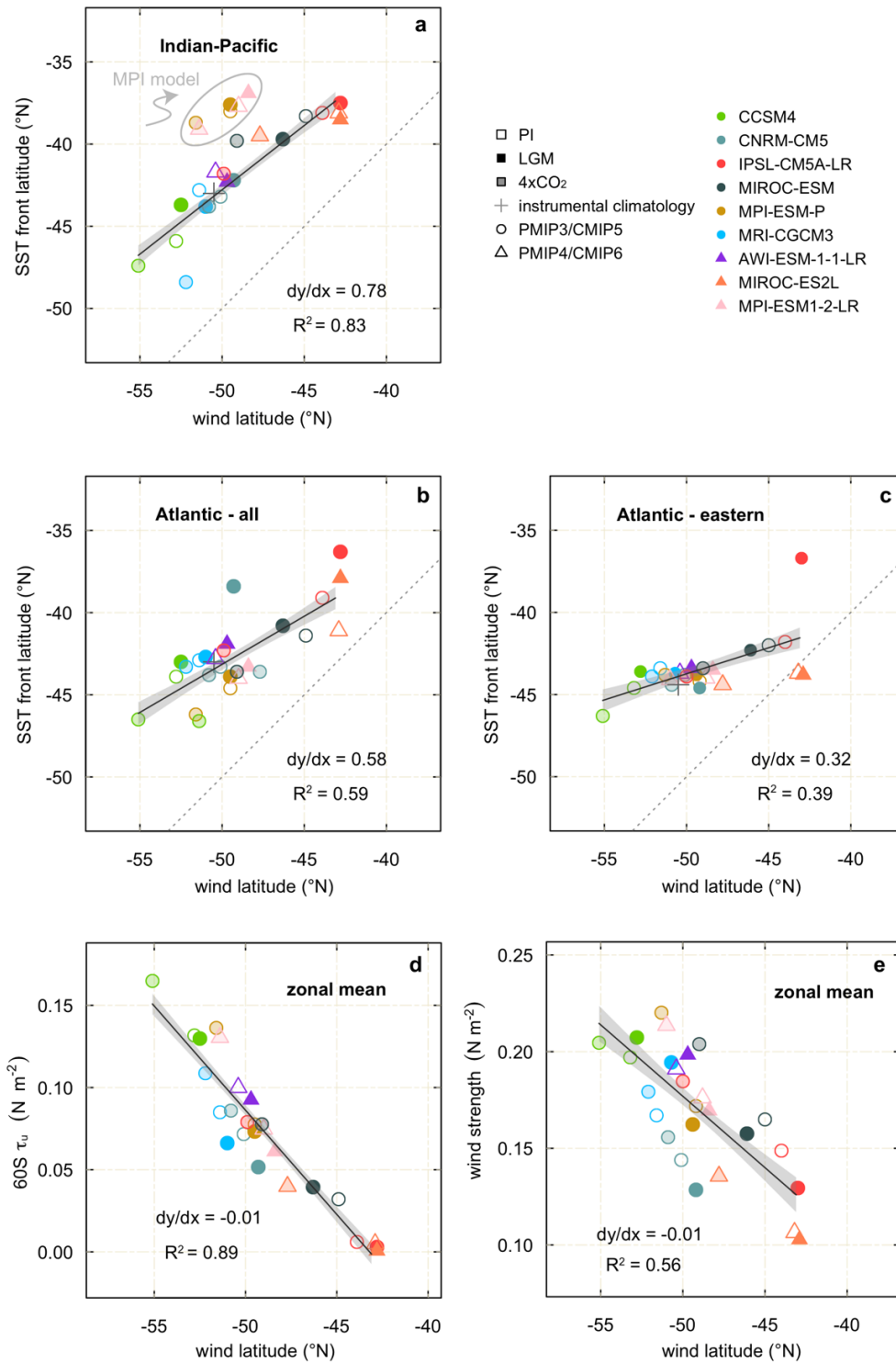


753  
754  
755  
756

**Extended Data 3. Atlantic meridional  $\delta^{18}\text{O}$  profiles.** As above, but for the Atlantic.

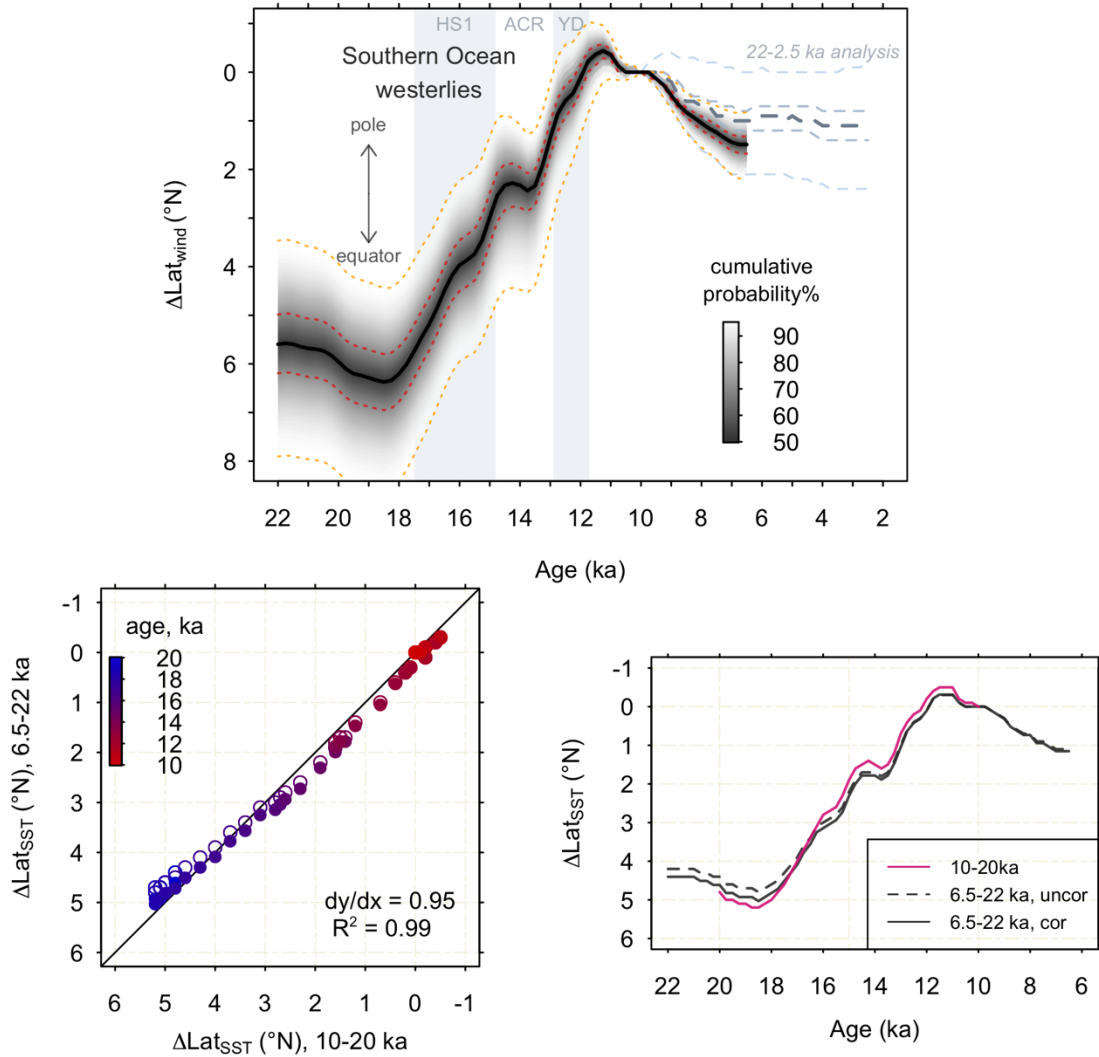


757  
 758 **Extended Data 4.  $\Delta\text{Lat}_{\text{SST}}$  within different sectors and core weightings in the Indian-Pacific**  
 759 **sectors.** Change in the SST front latitude ( $\Delta\text{Lat}_{\text{SST}}$ ) from 20-10 ka using (a) all data from across the  
 760 Southern Ocean, and in the (b) Indian-Pacific and (c) Atlantic sectors separately. The 5<sup>th</sup>, 32<sup>nd</sup>, 50<sup>th</sup>,  
 761 68<sup>th</sup>, and 95<sup>th</sup> percentiles are indicated. Contribution of each record to the Indian-Pacific  $\Delta\text{Lat}_{\text{SST}}$   
 762 reconstruction based on leave-one-out analysis (Methods). (d-e) 10-20 ka reconstruction (f-g) 6.5-22  
 763 ka reconstruction. Note Antarctic marginal sites from the Atlantic sector are also included given the  
 764 paucity of data from south of 65°S. Symbols distinguish species of planktic foraminifera (circles = *N.*  
 765 *pachyderma*, triangles = *G. bulloides*, squares = *G. ruber*).  
 766  
 767  
 768  
 769  
 770  
 771  
 772  
 773  
 774  
 775  
 776  
 777



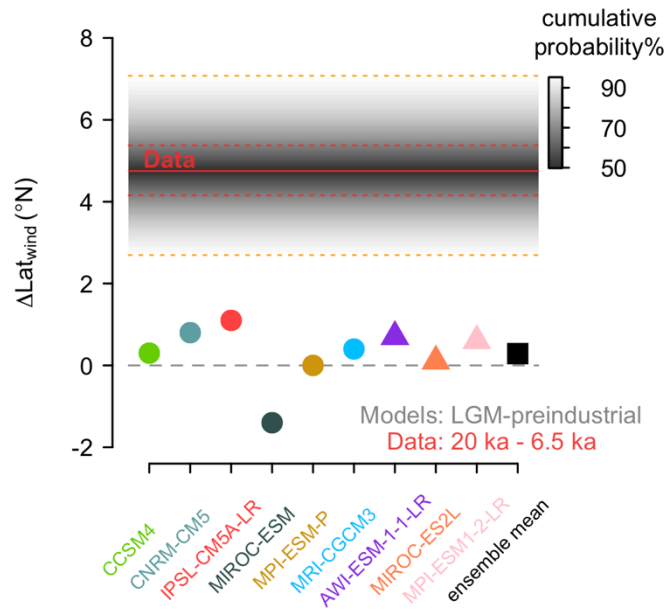
778  
 779  
 780  
 781  
 782  
 783  
 784  
 785  
 786  
 787  
 788

**Extended Data 5. PMIP3/4 and CMIP5/6 ensemble.** (a) Relationship between the wind latitude (latitude of maximum zonal-mean  $\tau_u$ ) and SST front latitude (latitude of maximum  $\partial SST/\partial Lat$ , averaged over a  $10^\circ$  latitudinal window) in the model ensemble across the Indian and Pacific sectors. The MPI model sits as an outlier from this the rest of the ensemble, possibly due to known SST temperature biases in the Indian Ocean<sup>113</sup>, and is excluded from the regression. Including the MPI model has a negligible impact on our results (Methods). (b) As (a) but for the Atlantic sector. (c) As (a) but for the eastern Atlantic sector, where the vast majority of the mid-latitude sites in the Atlantic are located. (d) Relationship between the wind latitude and zonal-mean wind stress at  $60^\circ S$  ( $60S \tau_u$ ) in the model ensemble (e) Relationship between the wind latitude and the wind strength (maximum zonal-mean  $\tau_u$ ) in the model ensemble.



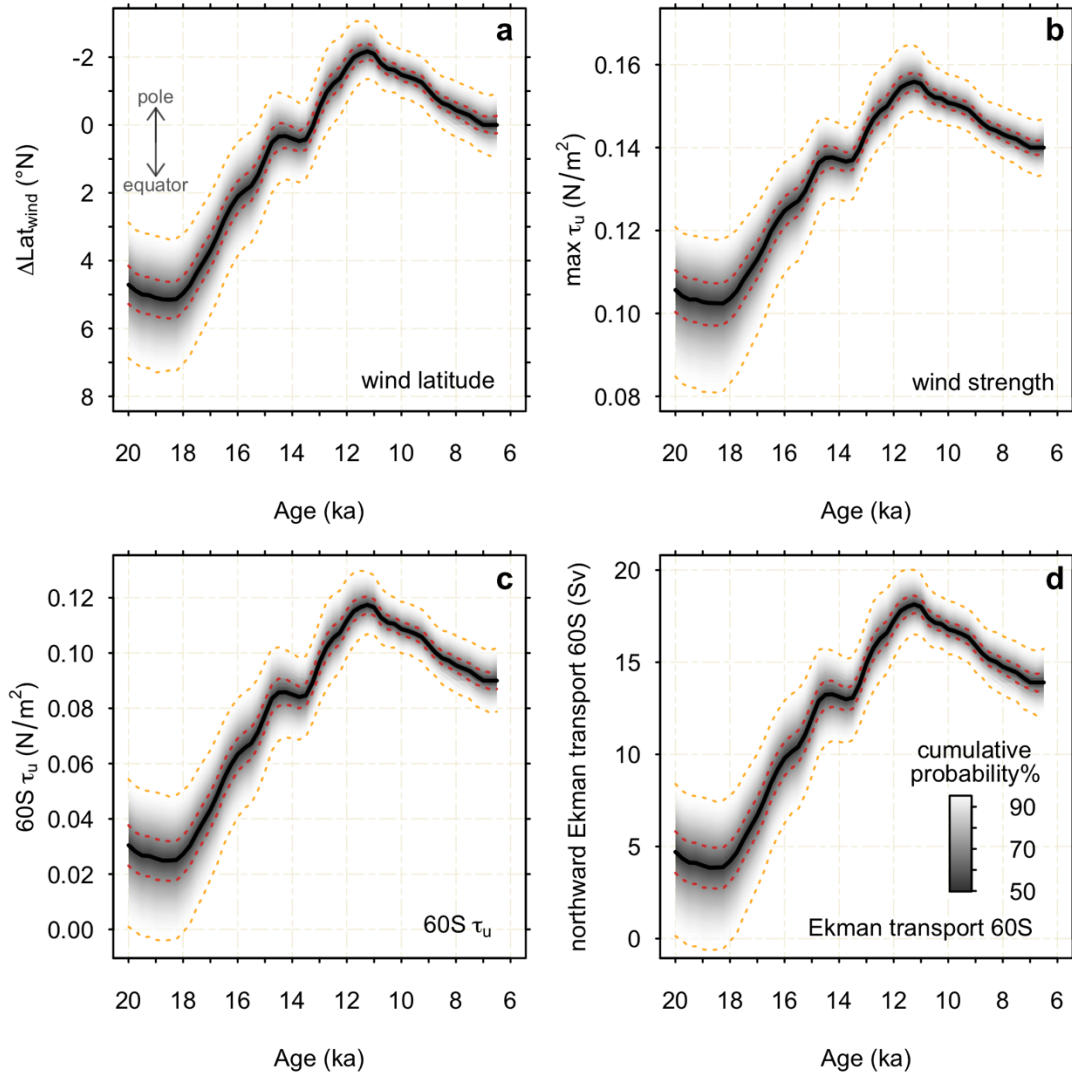
789  
 790  
 791  
 792  
 793  
 794  
 795  
 796  
 797  
 798  
 799  
 800  
 801

**Extended Data 6. 22-6.5 ka analysis. (top)** Changes in the wind latitude ( $\Delta\text{Lat}_{\text{wind}}$ ) from 22-6.5 ka. The higher uncertainties compared to the 20-10 ka reconstruction is due to the lower number of sites than span this interval. The 5<sup>th</sup>, 32<sup>nd</sup>, 50<sup>th</sup>, 68<sup>th</sup>, and 95<sup>th</sup> percentiles are indicated. The grey dashed line shows the same analysis extended to 2.5 ka; while the uncertainties are very large due to the limited number of cores than span this interval, the results indicate little change in the position of the wind latitude during the Holocene **(bottom)** Comparison of reconstructed Indian-Pacific  $\Delta\text{Lat}_{\text{SST}}$  using the 10-20 ka subset and 6.5-22 ka subset of cores. Open circles and the dashed grey curve correspond to the the 6.5-22 ka reconstruction uncorrected; filled circles and solid grey line correspond to the 6.5-22 ka reconstruction with a 1/0.95 correction applied (see Methods). The pink curve shows the 10-20 ka reconstruction.



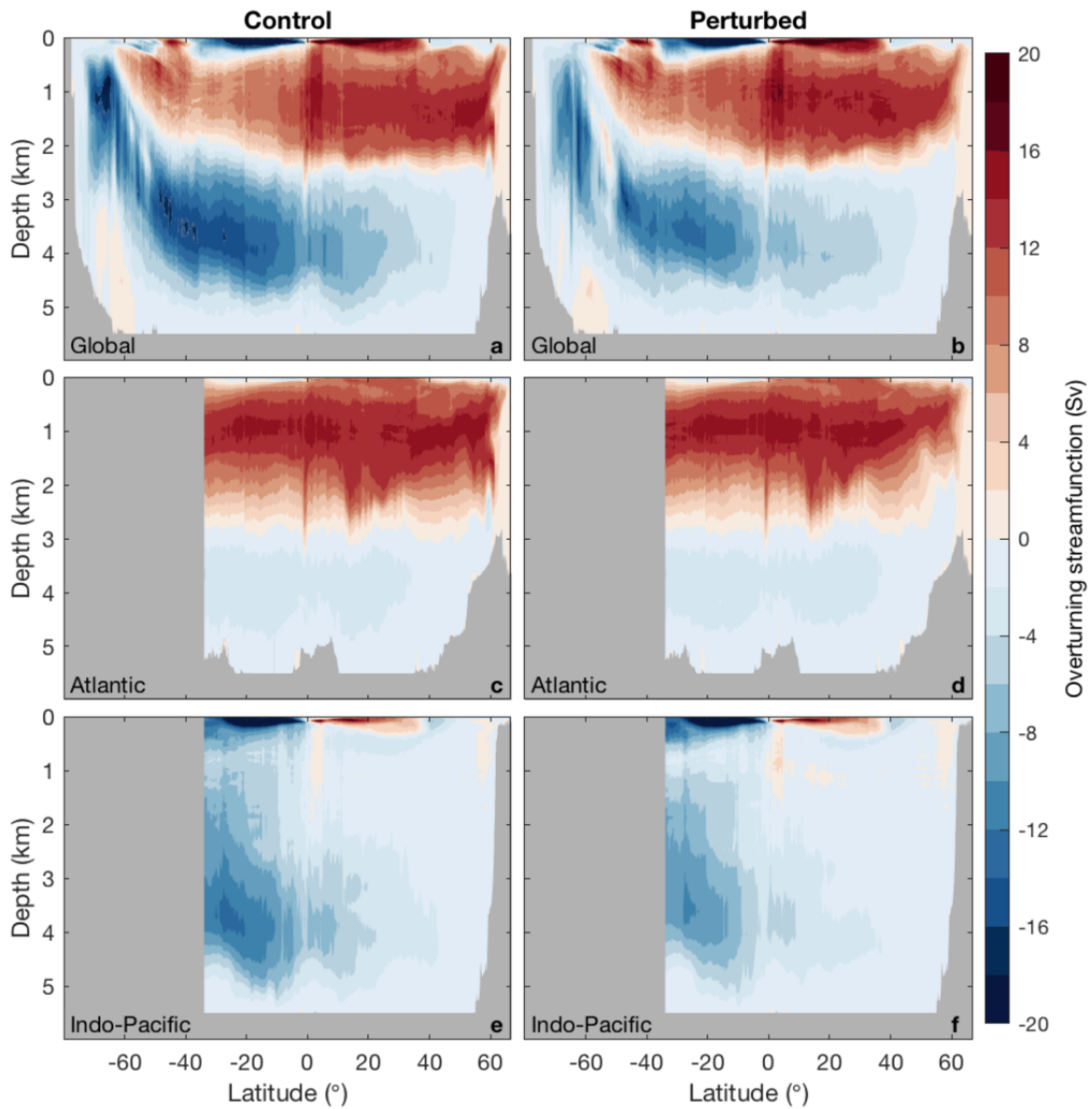
802  
803  
804  
805  
806

**Extended Data 7. LGM-PI change in the PMIP3/4 ensemble.** LGM-PI change in position of maximum zonal-mean zonal wind stress in the PIMP3 (circles) and PMIP4 (triangles) ensemble, compared to the reconstructed change in  $\Delta\text{Lat}_{\text{wind}}$  between 20-6.5 ka.



807  
808  
809  
810  
811  
812  
813  
814

**Extended Data 8. Deglacial changes in wind latitude, wind strength, wind stress at 60°S and northward Ekman transport at 60°S.** Reconstructed changes in (a) the wind latitude ( $\Delta\text{Lat}_{\text{wind}}$ ) (b) the wind strength ( $\text{max } \tau_u$ ) (c) zonal-mean wind stress at 60°S ( $60\text{S } \tau_u$ ) (d) northward Ekman transport at 60°S. (b) and (c) are calculated using the reconstructed changes in wind latitude (a) and the relationships between wind latitude and these parameters in the model ensemble (Extended Data Fig. 5). Northward Ekman transport at 60°S is calculated using zonal wind stress at 60°S (Methods).



815

816

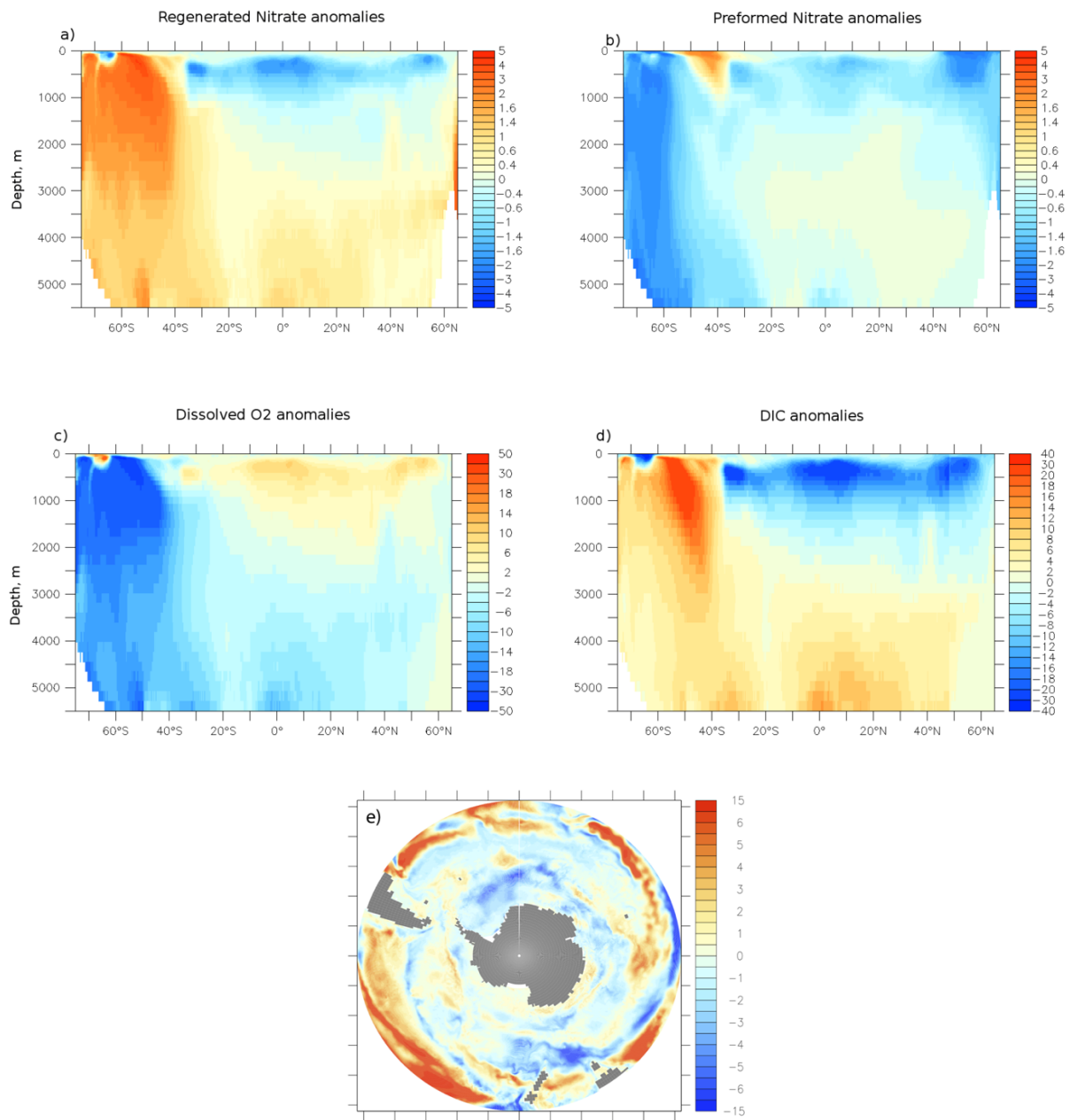
817

818

819

820

**Extended Data 9. MOM5-SIS-Wombat circulation results.** (a-f) Meridional overturning streamfunction in the Control (a,c,e) and Perturbed experiments (b,d,f), for the global ocean (a,b), Atlantic (c,d) and Indo-Pacific (e,f) oceans. (g) Zonally averaged mixed layer depth (MLD) in the Control (black) and Perturbed (red) simulations.



821

822  
 823  
 824  
 825  
 826  
 827  
 828

**Extended Data 10. MOM5-SIS-Wombat biogeochemical results.** Zonally averaged anomalies (Perturbed-Control) in **(a)** regenerated  $\text{NO}_3$  ( $\text{mmol}/\text{m}^3$ ), **(b)** preformed  $\text{NO}_3$  ( $\text{mmol}/\text{m}^3$ ), **(c)**  $\text{O}_2$  ( $\text{mmol}/\text{m}^3$ ), **and (d)** DIC ( $\text{mmol}/\text{m}^3$ ). **(e)** Vertically integrated (over the upper 149 m) gross phytoplankton production ( $\text{molC}/\text{m}^2/\text{yr}$ ) anomalies (Perturbed-Control).

829 **References**

- 830 1. Marshall, J. & Speer, K. Closure of the meridional overturning circulation through Southern Ocean  
831 upwelling. *Nat. Geosci.* **5**, 171–180 (2012).
- 832 2. Toggweiler, J. R., Russell, J. L. & Carson, S. R. Midlatitude westerlies, atmospheric CO<sub>2</sub>, and  
833 climate change during the ice ages. *Paleoceanography* **21**, (2006).
- 834 3. Sigman, D. M. & Boyle, E. A. Glacial/interglacial variations in atmospheric carbon dioxide. *Nature*  
835 **407**, 859–869 (2000).
- 836 4. Anderson, R. F. *et al.* Wind-Driven Upwelling in the Southern Ocean and the Deglacial Rise in  
837 Atmospheric CO<sub>2</sub>. *Science* **323**, 1443–1448 (2009).
- 838 5. Kohfeld, K. E. *et al.* Southern Hemisphere westerly wind changes during the Last Glacial  
839 Maximum: paleo-data synthesis. *Quat. Sci. Rev.* **68**, 76–95 (2013).
- 840 6. Sime, L. C. *et al.* Southern Hemisphere westerly wind changes during the Last Glacial Maximum:  
841 model-data comparison. *Quat. Sci. Rev.* **64**, 104–120 (2013).
- 842 7. Sime, L. C. *et al.* Sea ice led to poleward-shifted winds at the Last Glacial Maximum: the  
843 influence of state dependency on CMIP5 and PMIP3 models. *Clim. Past* **12**, 2241–2253 (2016).
- 844 8. Yin, J. H. A consistent poleward shift of the storm tracks in simulations of 21st century climate.  
845 *Geophys. Res. Lett.* **32**, (2005).
- 846 9. Chen, G., Lu, J. & Frierson, D. M. W. Phase Speed Spectra and the Latitude of Surface  
847 Westerlies: Interannual Variability and Global Warming Trend. *J. Clim.* **21**, 5942–5959 (2008).
- 848 10. Goyal, R., Gupta, A. S., Jucker, M. & England, M. H. Historical and Projected Changes in the  
849 Southern Hemisphere Surface Westerlies. *Geophys. Res. Lett.* **48**, e2020GL090849 (2021).
- 850 11. Toggweiler, J. R. & Samuels, B. Effect of drake passage on the global thermohaline circulation.  
851 *Deep Sea Res. Part Oceanogr. Res. Pap.* **42**, 477–500 (1995).
- 852 12. Abernathy, R., Marshall, J. & Ferreira, D. The Dependence of Southern Ocean Meridional  
853 Overturning on Wind Stress. *J. Phys. Oceanogr.* **41**, 2261–2278 (2011).
- 854 13. Martin, J. H., Gordon, R. M. & Fitzwater, S. E. Iron in Antarctic waters. *Nature* **345**, 156–158  
855 (1990).
- 856 14. Mitchell, B. G., Brody, E. A., Holm-Hansen, O., McClain, C. & Bishop, J. Light limitation of  
857 phytoplankton biomass and macronutrient utilization in the Southern Ocean. *Limnol. Oceanogr.*  
858 **36**, 1662–1677 (1991).

- 859 15. Ito, T. & Follows, M. J. Preformed phosphate, soft tissue pump and atmospheric CO<sub>2</sub>. *J. Mar.*  
860 *Res.* **63**, 813–839 (2005).
- 861 16. Toggweiler, J. R. Variation of atmospheric CO<sub>2</sub> by ventilation of the ocean's deepest water.  
862 *Paleoceanography* **14**, 571–588 (1999).
- 863 17. Lauderdale, J. M., Williams, R. G., Munday, D. R. & Marshall, D. P. The impact of Southern  
864 Ocean residual upwelling on atmospheric CO<sub>2</sub> on centennial and millennial timescales. *Clim.*  
865 *Dyn.* **48**, 1611–1631 (2017).
- 866 18. Ai, X. E. *et al.* Southern Ocean upwelling, Earth's obliquity, and glacial-interglacial atmospheric  
867 CO<sub>2</sub> change. *Science* **370**, 1348–1352 (2020).
- 868 19. Gray, W. R. *et al.* Wind-Driven Evolution of the North Pacific Subpolar Gyre Over the Last  
869 Deglaciation. *Geophys. Res. Lett.* **47**, e2019GL086328 (2020).
- 870 20. Kageyama, M. *et al.* The PMIP4-CMIP6 Last Glacial Maximum experiments: preliminary results  
871 and comparison with the PMIP3-CMIP5 simulations. *Clim. Past Discuss.* 1–37 (2020)  
872 doi:<https://doi.org/10.5194/cp-2019-169>.
- 873 21. Li, C. & Battisti, D. S. Reduced Atlantic Storminess during Last Glacial Maximum: Evidence from  
874 a Coupled Climate Model. *J. Clim.* **21**, 3561–3579 (2008).
- 875 22. Chavaillaz, Y., Codron, F. & Kageyama, M. Southern westerlies in LGM and future (RCP4.5)  
876 climates. *Clim. Past* **9**, 517–524 (2013).
- 877 23. Buizert, C. *et al.* Abrupt ice-age shifts in southern westerly winds and Antarctic climate forced  
878 from the north. *Nature* **563**, 681–685 (2018).
- 879 24. Bereiter, B. *et al.* Revision of the EPICA Dome C CO<sub>2</sub> record from 800 to 600 kyr before present.  
880 *Geophys. Res. Lett.* **42**, 542–549 (2015).
- 881 25. Dong, S., Sprintall, J. & Gille, S. T. Location of the Antarctic Polar Front from AMSR-E Satellite  
882 Sea Surface Temperature Measurements. *J. Phys. Oceanogr.* **36**, 2075–2089 (2006).
- 883 26. Yang, H. *et al.* Tropical Expansion Driven by Poleward Advancing Midlatitude Meridional  
884 Temperature Gradients. *J. Geophys. Res. Atmospheres* **125**, e2020JD033158 (2020).
- 885 27. Gnanadesikan, A. & Hallberg, R. W. On the Relationship of the Circumpolar Current to Southern  
886 Hemisphere Winds in Coarse-Resolution Ocean Models. *J. Phys. Oceanogr.* **30**, 2013–2034  
887 (2000).

- 888 28. Gordon, A. L., Molinelli, E. & Baker, T. Large-scale relative dynamic topography of the Southern  
889 Ocean. *J. Geophys. Res. Oceans* **83**, 3023–3032 (1978).
- 890 29. Gherardi, J.-M. *et al.* Glacial-interglacial circulation changes inferred from <sup>231</sup>Pa/<sup>230</sup>Th  
891 sedimentary record in the North Atlantic region. *Paleoceanography* **24**, (2009).
- 892 30. Stocker, T. F. & Johnsen, S. J. A minimum thermodynamic model for the bipolar seesaw.  
893 *Paleoceanography* **18**, (2003).
- 894 31. Shakun, J. D. *et al.* Global warming preceded by increasing carbon dioxide concentrations during  
895 the last deglaciation. *Nature* **484**, 49–54 (2012).
- 896 32. Gottschalk, J. *et al.* Mechanisms of millennial-scale atmospheric CO<sub>2</sub> change in numerical model  
897 simulations. *Quat. Sci. Rev.* **220**, 30–74 (2019).
- 898 33. Menviel, L. *et al.* Southern Hemisphere westerlies as a driver of the early deglacial atmospheric  
899 CO<sub>2</sub> rise. *Nat. Commun.* **9**, 2503 (2018).
- 900 34. Hogg, A. M., Spence, P., Saenko, O. A. & Downes, S. M. The Energetics of Southern Ocean  
901 Upwelling. *J. Phys. Oceanogr.* **47**, 135–153 (2017).
- 902 35. Spence, P., Saenko, O. A., Eby, M. & Weaver, A. J. The Southern Ocean Overturning:  
903 Parameterized versus Permitted Eddies. *J. Phys. Oceanogr.* **39**, 1634–1651 (2009).
- 904 36. Hallberg, R. & Gnanadesikan, A. The Role of Eddies in Determining the Structure and Response  
905 of the Wind-Driven Southern Hemisphere Overturning: Results from the Modeling Eddies in the  
906 Southern Ocean (MESO) Project. *J. Phys. Oceanogr.* **36**, 2232–2252 (2006).
- 907 37. Boyle, E. A. Vertical oceanic nutrient fractionation and glacial/interglacial CO<sub>2</sub> cycles. *Nature*  
908 **331**, 55–56 (1988).
- 909 38. Du, J., Haley, B. A. & Mix, A. C. Evolution of the Global Overturning Circulation since the Last  
910 Glacial Maximum based on marine authigenic neodymium isotopes. *Quat. Sci. Rev.* **241**, 106396  
911 (2020).
- 912 39. Rae, J. W. B. *et al.* CO<sub>2</sub> storage and release in the deep Southern Ocean on millennial to  
913 centennial timescales. *Nature* **562**, 569–573 (2018).
- 914 40. Jaccard, S. L. & Galbraith, E. D. Large climate-driven changes of oceanic oxygen concentrations  
915 during the last deglaciation. *Nat. Geosci.* **5**, 151–156 (2012).
- 916 41. Hoogakker, B. A. A. *et al.* Glacial expansion of oxygen-depleted seawater in the eastern tropical  
917 Pacific. *Nature* **562**, 410–413 (2018).

- 918 42. Peterson, C. D. & Lisiecki, L. E. Deglacial carbon cycle changes observed in a compilation of 127  
919 benthic  $\delta^{13}\text{C}$  time series (20–6&thinsp;ka). *Clim. Past* **14**, 1229–1252 (2018).
- 920 43. Jaccard, S. L. *et al.* Two Modes of Change in Southern Ocean Productivity Over the Past Million  
921 Years. *Science* **339**, 1419–1423 (2013).
- 922 44. Bishop, S. P. *et al.* Southern Ocean Overturning Compensation in an Eddy-Resolving Climate  
923 Simulation. *J. Phys. Oceanogr.* **46**, 1575–1592 (2016).
- 924 45. Dufour, C. O. *et al.* Role of Mesoscale Eddies in Cross-Frontal Transport of Heat and  
925 Biogeochemical Tracers in the Southern Ocean. *J. Phys. Oceanogr.* **45**, 3057–3081 (2015).
- 926 46. Burke, A. & Robinson, L. F. The Southern Ocean’s Role in Carbon Exchange During the Last  
927 Deglaciation. *Science* **335**, 557–561 (2012).
- 928 47. Martínez-Botí, M. A. *et al.* Boron isotope evidence for oceanic carbon dioxide leakage during the  
929 last deglaciation. *Nature* **518**, 219–222 (2015).
- 930 48. Menviel, L. & Joos, F. Toward explaining the Holocene carbon dioxide and carbon isotope  
931 records: Results from transient ocean carbon cycle-climate simulations. *Paleoceanography* **27**,  
932 (2012).
- 933 49. Fogwill, C. J., Turney, C. S. M., Hutchinson, D. K., Taschetto, A. S. & England, M. H. Obliquity  
934 Control On Southern Hemisphere Climate During The Last Glacial. *Sci. Rep.* **5**, 11673 (2015).
- 935 50. Gruber, N., Landschützer, P. & Lovenduski, N. S. The Variable Southern Ocean Carbon Sink.  
936 *Annu. Rev. Mar. Sci.* **11**, 159–186 (2019).
- 937 51. Kalnay, E. *et al.* The NCEP/NCAR 40-Year Reanalysis Project. *Bull. Am. Meteorol. Soc.* **77**, 437–  
938 472 (1996).
- 939 52. Haddam, N. A., Michel, E., Siani, G., Licari, L. & Dewilde, F. Ventilation and Expansion of  
940 Intermediate and Deep Waters in the Southeast Pacific During the Last Termination.  
941 *Paleoceanogr. Paleoclimatology* **35**, e2019PA003743 (2020).
- 942 53. Gottschalk, J. *et al.* Glacial heterogeneity in Southern Ocean carbon storage abated by fast South  
943 Indian deglacial carbon release. *Nat. Commun.* **11**, 6192 (2020).
- 944 54. Sarin, M. *et al.* Changes in East Atlantic Deepwater Circulation over the last 30,000 years:  
945 Eight time slice reconstructions. *Paleoceanography* **9**, 209–267 (1994).

- 946 55. Wang, Y. V. *et al.* Northern and southern hemisphere controls on seasonal sea surface  
947 temperatures in the Indian Ocean during the last deglaciation. *Paleoceanography* **28**, 619–632  
948 (2013).
- 949 56. Stuut, J.-B. W. *et al.* A 300-kyr record of aridity and wind strength in southwestern Africa:  
950 inferences from grain-size distributions of sediments on Walvis Ridge, SE Atlantic. *Mar. Geol.*  
951 **180**, 221–233 (2002).
- 952 57. Levi, C. *et al.* Low-latitude hydrological cycle and rapid climate changes during the last  
953 deglaciation. *Geochem. Geophys. Geosystems* **8**, (2007).
- 954 58. Schneider, R. R., Müller, P. J. & Ruhland, G. Late Quaternary surface circulation in the east  
955 equatorial South Atlantic: Evidence from Alkenone sea surface temperatures. *Paleoceanography*  
956 **10**, 197–219 (1995).
- 957 59. Stuut, J.-B. W. *et al.* A 5.3-Million-Year History of Monsoonal Precipitation in Northwestern  
958 Australia. *Geophys. Res. Lett.* **46**, 6946–6954 (2019).
- 959 60. Bostock, H. C., Opdyke, B. N., Gagan, M. K. & Fifield, L. K. Carbon isotope evidence for changes  
960 in Antarctic Intermediate Water circulation and ocean ventilation in the southwest Pacific during  
961 the last deglaciation. *Paleoceanography* **19**, (2004).
- 962 61. Santos, T. P. *et al.* Prolonged warming of the Brazil Current precedes deglaciations. *Earth Planet.*  
963 *Sci. Lett.* **463**, 1–12 (2017).
- 964 62. Caley, T. *et al.* High-latitude obliquity as a dominant forcing in the Agulhas current system. *Clim.*  
965 *Past* **7**, 1285–1296 (2011).
- 966 63. Portilho-Ramos, R. C. *et al.* Methane release from the southern Brazilian margin during the last  
967 glacial. *Sci. Rep.* **8**, 5948 (2018).
- 968 64. Pereira, L. S., Arz, H. W., Pätzold, J. & Portilho-Ramos, R. C. Productivity Evolution in the South  
969 Brazilian Bight During the Last 40,000 Years. *Paleoceanogr. Paleoclimatology* **33**, 1339–1356  
970 (2018).
- 971 65. Carlson, A. E. *et al.* Subtropical Atlantic salinity variability and Atlantic meridional circulation  
972 during the last deglaciation. *Geology* **36**, 991–994 (2008).
- 973 66. Scussolini, P. & Peeters, F. J. C. A record of the last 460 thousand years of upper ocean  
974 stratification from the central Walvis Ridge, South Atlantic. *Paleoceanography* **28**, 426–439  
975 (2013).

- 976 67. Chiessi, C. M. *et al.* Variability of the Brazil Current during the late Holocene. *Palaeogeogr.*  
977 *Palaeoclimatol. Palaeoecol.* **415**, 28–36 (2014).
- 978 68. Winn, K. Carbon and oxygen isotope ratios on planktonic foraminifera in subtropical Southeast  
979 Pacific core GIK17747-2. 333 data points (2013) doi:10.1594/PANGAEA.815877.
- 980 69. Mohtadi, M. *et al.* Deglacial pattern of circulation and marine productivity in the upwelling region  
981 off central-south Chile. *Earth Planet. Sci. Lett.* **272**, 221–230 (2008).
- 982 70. Dyez, K. A., Zahn, R. & Hall, I. R. Multicentennial Agulhas leakage variability and links to North  
983 Atlantic climate during the past 80,000 years. *Paleoceanography* **29**, 1238–1248 (2014).
- 984 71. Schiraldi, B., Sikes, E. L., Elmore, A. C., Cook, M. S. & Rose, K. A. Southwest Pacific subtropics  
985 responded to last deglacial warming with changes in shallow water sources. *Paleoceanography*  
986 **29**, 595–611 (2014).
- 987 72. Martínez-Méndez, G. *et al.* Contrasting multiproxy reconstructions of surface ocean hydrography  
988 in the Agulhas Corridor and implications for the Agulhas Leakage during the last 345,000 years.  
989 *Paleoceanography* **25**, (2010).
- 990 73. Calvo, E., Pelejero, C., Deckker, P. D. & Logan, G. A. Antarctic deglacial pattern in a 30 kyr  
991 record of sea surface temperature offshore South Australia. *Geophys. Res. Lett.* **34**, (2007).
- 992 74. Nelson, C. S., Hendy, I. L., Neil, H. L., Hendy, C. H. & Weaver, P. P. E. Last glacial jetting of cold  
993 waters through the Subtropical Convergence zone in the Southwest Pacific off eastern New  
994 Zealand, and some geological implications. *Palaeogeogr. Palaeoclimatol. Palaeoecol.* **156**, 103–  
995 121 (2000).
- 996 75. Gottschalk, J. *et al.* Past Carbonate Preservation Events in the Deep Southeast Atlantic Ocean  
997 (Cape Basin) and Their Implications for Atlantic Overturning Dynamics and Marine Carbon  
998 Cycling. *Paleoceanogr. Paleoclimatology* **33**, 643–663 (2018).
- 999 76. Lamy, F. *et al.* Antarctic Timing of Surface Water Changes off Chile and Patagonian Ice Sheet  
1000 Response. *Science* **304**, 1959–1962 (2004).
- 1001 77. Haddam, N. A. *et al.* Changes in latitudinal sea surface temperature gradients along the Southern  
1002 Chilean margin since the last glacial. *Quat. Sci. Rev.* **194**, 62–76 (2018).
- 1003 78. Hodell, D. A., Venz, K. A., Charles, C. D. & Ninnemann, U. S. Pleistocene vertical carbon isotope  
1004 and carbonate gradients in the South Atlantic sector of the Southern Ocean. *Geochem. Geophys.*  
1005 *Geosystems* **4**, 1–19 (2003).

- 1006 79. Pichon, J.-J. *et al.* Surface water temperature changes in the high latitudes of the southern  
1007 hemisphere over the Last Glacial-Interglacial Cycle. *Paleoceanography* **7**, 289–318 (1992).
- 1008 80. Rickaby, R. E. M. & Elderfield, H. Planktonic foraminiferal Cd/Ca: Paleonutrients or  
1009 paleotemperature? *Paleoceanography* **14**, 293–303 (1999).
- 1010 81. Gottschalk, J., Skinner, L. C. & Waelbroeck, C. Contribution of seasonal sub-Antarctic surface  
1011 water variability to millennial-scale changes in atmospheric CO<sub>2</sub> over the last deglaciation and  
1012 Marine Isotope Stage 3. *Earth Planet. Sci. Lett.* **411**, 87–99 (2015).
- 1013 82. Sikes, E. L. *et al.* Southern Ocean seasonal temperature and Subtropical Front movement on the  
1014 South Tasman Rise in the late Quaternary. *Paleoceanography* **24**, (2009).
- 1015 83. Sicre, M. A. *et al.* Mid-latitude Southern Indian Ocean response to Northern Hemisphere Heinrich  
1016 events. *Earth Planet. Sci. Lett.* **240**, 724–731 (2005).
- 1017 84. Labeyrie, L. *et al.* Hydrographic changes of the Southern Ocean (southeast Indian Sector) Over  
1018 the last 230 kyr. *Paleoceanography* **11**, 57–76 (1996).
- 1019 85. Govin, A. *et al.* Evidence for northward expansion of Antarctic Bottom Water mass in the  
1020 Southern Ocean during the last glacial inception. *Paleoceanography* **24**, (2009).
- 1021 86. Bostock, H. C., Hayward, B. W., Neil, H. L., Sabaa, A. T. & Scott, G. H. Changes in the position of  
1022 the Subtropical Front south of New Zealand since the last glacial period. *Paleoceanography* **30**,  
1023 824–844 (2015).
- 1024 87. Hodell, D. A., Charles, C. D. & Ninnemann, U. S. Comparison of interglacial stages in the South  
1025 Atlantic sector of the southern ocean for the past 450 kyr: implications for Marine Isotope Stage  
1026 (MIS) 11. *Glob. Planet. Change* **24**, 7–26 (2000).
- 1027 88. Charles, C. D., Froelich, P. N., Zibello, M. A., Mortlock, R. A. & Morley, J. J. Biogenic opal in  
1028 Southern Ocean sediments over the last 450,000 years: Implications for surface water chemistry  
1029 and circulation. *Paleoceanography* **6**, 697–728 (1991).
- 1030 89. *Use of Proxies in Paleoceanography: Examples from the South Atlantic.* (Springer-Verlag, 1999).  
1031 doi:10.1007/978-3-642-58646-0.
- 1032 90. Caniupán, M. *et al.* Millennial-scale sea surface temperature and Patagonian Ice Sheet changes  
1033 off southernmost Chile (53°S) over the past ~60 kyr. *Paleoceanography* **26**, (2011).
- 1034 91. Hasenfratz, A. P. *et al.* The residence time of Southern Ocean surface waters and the 100,000-  
1035 year ice age cycle. *Science* **363**, 1080–1084 (2019).

- 1036 92. *Proceedings of the Ocean Drilling Program, 177 Scientific Results*. vol. 177 (Ocean Drilling  
1037 Program, 2003).
- 1038 93. Mashiotta, T. A., Lea, D. W. & Spero, H. J. Glacial–interglacial changes in Subantarctic sea  
1039 surface temperature and  $\delta^{18}\text{O}$ -water using foraminiferal Mg. *Earth Planet. Sci. Lett.* **170**, 417–  
1040 432 (1999).
- 1041 94. Crosta, X., Sturm, A., Armand, L. & Pichon, J.-J. Late Quaternary sea ice history in the Indian  
1042 sector of the Southern Ocean as recorded by diatom assemblages. *Mar. Micropaleontol.* **50**,  
1043 209–223 (2004).
- 1044 95. *Carbon Cycling in the Glacial Ocean: Constraints on the Ocean's Role in Global Change:  
1045 Quantitative Approaches in Paleoceanography*. (Springer-Verlag, 1994). doi:10.1007/978-3-642-  
1046 78737-9.
- 1047 96. Grobe, H. & Mackensen, A. Late Quaternary climatic cycles as recorded in sediments from the  
1048 Antarctic continental margin. in *Antarctic Research Series* (eds. Kennett, J. P. & Warkne, D. A.)  
1049 vol. 56 349–376 (American Geophysical Union, 1992).
- 1050 97. Lu, Z. *et al.* Oxygen depletion recorded in upper waters of the glacial Southern Ocean. *Nat.*  
1051 *Commun.* **7**, 11146 (2016).
- 1052 98. LeGrande, A. N. & Schmidt, G. A. Global gridded data set of the oxygen isotopic composition in  
1053 seawater. *Geophys. Res. Lett.* **33**, L12604 (2006).
- 1054 99. Wood, S. N. Fast stable restricted maximum likelihood and marginal likelihood estimation of  
1055 semiparametric generalized linear models. *J. R. Stat. Soc. Ser. B Stat. Methodol.* **73**, 3–36  
1056 (2011).
- 1057 100. Wood, S. N., Pya, N. & Säfken, B. Smoothing Parameter and Model Selection for General  
1058 Smooth Models. *J. Am. Stat. Assoc.* **111**, 1548–1563 (2016).
- 1059 101. Simpson, G. L. Modelling Palaeoecological Time Series Using Generalised Additive Models.  
1060 *Front. Ecol. Evol.* **6**, (2018).
- 1061 102. Schrag, D. P. *et al.* The oxygen isotopic composition of seawater during the Last Glacial  
1062 Maximum. *Quat. Sci. Rev.* **21**, 331–342 (2002).
- 1063 103. Lambeck, K., Rouby, H., Purcell, A., Sun, Y. & Sambridge, M. Sea level and global ice  
1064 volumes from the Last Glacial Maximum to the Holocene. *Proc. Natl. Acad. Sci.* **111**, 15296–  
1065 15303 (2014).

- 1066 104. Kim, S.-T. & O'Neil, J. R. Equilibrium and nonequilibrium oxygen isotope effects in synthetic  
1067 carbonates. *Geochim. Cosmochim. Acta* **61**, 3461–3475 (1997).
- 1068 105. Malevich, S. B., Vetter, L. & Tierney, J. E. Global Core Top Calibration of  $\delta^{18}\text{O}$  in Planktic  
1069 Foraminifera to Sea Surface Temperature. *Paleoceanogr. Paleoclimatology* **34**, 1292–1315  
1070 (2019).
- 1071 106. Efron, B. Bootstrap Methods: Another Look at the Jackknife. *Ann. Stat.* **7**, 1–26 (1979).
- 1072 107. Saunders, K. M. *et al.* Holocene dynamics of the Southern Hemisphere westerly winds and  
1073 possible links to CO<sub>2</sub> outgassing. *Nat. Geosci.* **11**, 650–655 (2018).
- 1074 108. Lombard, F. *et al.* Modelling planktic foraminifer growth and distribution using an  
1075 ecophysiological multi-species approach. *Biogeosciences* **8**, 853–873 (2011).
- 1076 109. Braconnot, P. *et al.* Evaluation of climate models using palaeoclimatic data. *Nat. Clim.*  
1077 *Change* **2**, 417–424 (2012).
- 1078 110. Kageyama, M. *et al.* The PMIP4 contribution to CMIP6 – Part 1: Overview and over-arching  
1079 analysis plan. *Geosci. Model Dev.* **11**, 1033–1057 (2018).
- 1080 111. Taylor, K. E., Stouffer, R. J. & Meehl, G. A. An Overview of CMIP5 and the Experiment  
1081 Design. *Bull. Am. Meteorol. Soc.* **93**, 485–498 (2012).
- 1082 112. Eyring, V. *et al.* Overview of the Coupled Model Intercomparison Project Phase 6 (CMIP6)  
1083 experimental design and organization. *Geosci. Model Dev.* **9**, 1937–1958 (2016).
- 1084 113. Fathrio, I. *et al.* Assessment of western Indian Ocean SST bias of CMIP5 models. *J.*  
1085 *Geophys. Res. Oceans* **122**, 3123–3140 (2017).
- 1086 114. Chapman, C. C., Lea, M.-A., Meyer, A., Sallée, J.-B. & Hindell, M. Defining Southern Ocean  
1087 fronts and their influence on biological and physical processes in a changing climate. *Nat. Clim.*  
1088 *Change* **10**, 209–219 (2020).
- 1089 115. Barnes, E. A. & Polvani, L. Response of the Midlatitude Jets, and of Their Variability, to  
1090 Increased Greenhouse Gases in the CMIP5 Models. *J. Clim.* **26**, 7117–7135 (2013).
- 1091 116. McGraw, M. C. & Barnes, E. A. Seasonal Sensitivity of the Eddy-Driven Jet to Tropospheric  
1092 Heating in an Idealized AGCM. *J. Clim.* **29**, 5223–5240 (2016).
- 1093 117. Sigl, M. *et al.* The WAIS Divide deep ice core WD2014 chronology – Part 2: Annual-layer  
1094 counting (0–31 ka BP). *Clim. Past* **12**, 769–786 (2016).

- 1095 118. Olsen, A. *et al.* The Global Ocean Data Analysis Project version 2 (GLODAPv2) – an  
1096 internally consistent data product for the world ocean. *Earth Syst. Sci. Data* **8**, 297–323 (2016).
- 1097 119. Griffies, S. M. *et al.* Coordinated Ocean-ice Reference Experiments (COREs). *Ocean Model.*  
1098 **26**, 1–46 (2009).
- 1099 120. Redi, M. H. Oceanic Isopycnal Mixing by Coordinate Rotation. *J. Phys. Oceanogr.* **12**, 1154–  
1100 1154 (1982).
- 1101 121. Gent, P. R. & McWilliams, J. C. Isopycnal Mixing in Ocean Circulation Models. *J. Phys.*  
1102 *Oceanogr.* **20**, 150–155 (1990).
- 1103 122. Jackett, D. & McDougall, T. A Neutral Density Variable for the World’s Oceans. (1997)  
1104 doi:10.1175/1520-0485(1997)027<0237:ANDVFT>2.0.CO;2.
- 1105 123. Zika, J. D., England, M. H. & Sijp, W. P. The Ocean Circulation in Thermohaline Coordinates.  
1106 *J. Phys. Oceanogr.* **42**, 708–724 (2012).
- 1107 124. Boyle, E. A. The role of vertical chemical fractionation in controlling late Quaternary  
1108 atmospheric carbon dioxide. *J. Geophys. Res. Oceans* **93**, 15701–15714 (1988).
- 1109 125. Boyer, T. P. *et al.* World ocean database 2013. (2013) doi:10.7289/V5NZ85MT.
- 1110 126. AVISO: Satellite derived Sea Surface Height above Geoid | NCAR - Climate Data Guide.  
1111 [https://climatedataguide.ucar.edu/climate-data/aviso-satellite-derived-sea-surface-height-above-](https://climatedataguide.ucar.edu/climate-data/aviso-satellite-derived-sea-surface-height-above-geoid)  
1112 [geoid.](https://climatedataguide.ucar.edu/climate-data/aviso-satellite-derived-sea-surface-height-above-geoid)